Article

Skin-integrated wireless haptic interfaces for virtual and augmented reality

https://doi.org/10.1038/s41586-019-1687-0

Received: 9 January 2019

Accepted: 2 September 2019

Published online: 20 November 2019

Xinge Yu[1,23], Zhaoqian Xie[1,2,3,4,5,23], Yang Yu[6,7,8,23], Jungyup Lee[9,23], Abraham Vazquez-Guardado[10], Haiwen Luan[10], Jasper Ruban[9], Xin Ning[11], Aadeel Akhtar[12], Dengfeng Li[1], Bowen Ji[3,4,5,13], Yiming Liu[1], Rujie Sun[14], Jingyue Cao[15], Qingze Huo[3,4,5], Yishan Zhong[6,7], ChanMi Lee[6,7], SeungYeop Kim[6,7], Philipp Gutruf[16], Changxing Zhang[17], Yeguang Xue[3,4,5], Qinglei Guo[18], Aditya Chempakasseril[6,7], Peilin Tian[6,7], Wei Lu[10], JiYoon Jeong[9], YongJoon Yu[9], Jesse Cornman[12], CheeSim Tan[12], BongHoon Kim[6,7,10], KunHyuk Lee[10], Xue Feng[17], Yonggang Huang[3,4,5,10]* & John A. Rogers[4,5,6,7,10,19,20,21,22]*

Traditional technologies for virtual reality (VR) and augmented reality (AR) create human experiences through visual and auditory stimuli that replicate sensations associated with the physical world. The most widespread VR and AR systems use head-mounted displays, accelerometers and loudspeakers as the basis for three-dimensional, computer-generated environments that can exist in isolation or as overlays on actual scenery. In comparison to the eyes and the ears, the skin is a relatively underexplored sensory interface for VR and AR technology that could, nevertheless, greatly enhance experiences at a qualitative level, with direct relevance in areas such as communications, entertainment and medicine[1,2]. Here we present a wireless, battery-free platform of electronic systems and haptic (that is, touch-based) interfaces capable of softly laminating onto the curved surfaces of the skin to communicate information via spatio-temporally programmable patterns of localized mechanical vibrations. We describe the materials, device structures, power delivery strategies and communication schemes that serve as the foundations for such platforms. The resulting technology creates many opportunities for use where the skin provides an electronically programmable communication and sensory input channel to the body, as demonstrated through applications in social media and personal engagement, prosthetic control and feedback, and gaming and entertainment.

An important future for VR/AR lies in the development of a full, immersive experience that includes not only interactive images and sounds, but also sensations of touch. The consequences of technologies with multi-sensory capabilities of this type will be far reaching, across fields ranging from social media and communications, to gaming and entertainment, and to clinical medicine, rehabilitation and recovery[1,2]. The skin is the largest organ of the body, and mechanoreceptors distributed across the skin, within the dermis, form the basis of our physical interactions with the world. Specifically, responses to spatio-temporal patterns of force on the skin transmit to the brain as signals that define a mechanical sense of our surroundings[3–5]. Efforts to integrate electronically programmable interfaces to mechanoreceptors within a comprehensive VR/AR platform are, however, in their infancy compared to those associated with video and audio interfaces. Some approaches rely on collections of wired electrodes pressed against the skin to induce artificial, vibration-like sensations via electrostimulation, known as electrotactile effects[4,6,7]. Variability of the impedance of the skin across the body and between individuals, along with time dependent drifts in this quantity due to changes in the properties of the skin or the electrode surfaces, represent confounding challenges in selecting appropriate combinations of voltages and currents that create desired responses without pain or electrically induced lesions[8]. A promising alternative relies on mechanical forces, in the form of vibratory actuation imparted to the skin by electrical motors or piezoelectric devices, where relays, bulk wires and battery packs couple loosely to the body through textiles, tapes and straps to provide the necessary control

[1]Department of Biomedical Engineering, City University of Hong Kong, Hong Kong, China. [2]Department of Engineering Mechanics, Dalian University of Technology, Dalian, China. [3]Department of Civil and Environmental Engineering, Northwestern University, Evanston, IL, USA. [4]Department of Mechanical Engineering, Northwestern University, Evanston, IL, USA. [5]Department of Materials Science and Engineering, Northwestern University, Evanston, IL, USA. [6]Department of Materials Science and Engineering, University of Illinois at Urbana-Champaign, Urbana, IL, USA. [7]Frederick Seitz Materials Research Laboratory, University of Illinois at Urbana-Champaign, Urbana, IL, USA. [8]School of Materials Science and Engineering, Tsinghua University, Beijing, China. [9]NeuroLux Corporation, Evanston, IL, USA. [10]Simpson Querrey Institute, Center for Bio-Integrated Electronics, Northwestern University, Evanston, IL, USA. [11]Department of Aerospace Engineering, Pennsylvania State University, University Park, PA, USA. [12]PSYONIC, Inc., Champaign, IL, USA. [13]Department of Micro/Nano Electronics, Shanghai Jiao Tong University, Shanghai, China. [14]Bristol Composites Institute, University of Bristol, Bristol, UK. [15]Wearifi, Inc., Evanston, IL, USA. [16]Department of Biomedical Engineering, University of Arizona, Tucson, AZ, USA. [17]AML, Department of Engineering Mechanics, Interdisciplinary Research Center for Flexible Electronics Technology, Tsinghua University, Beijing, China. [18]School of Microelectronics, Shandong University, Jinan, China. [19]Department of Biomedical Engineering, Northwestern University, Evanston, IL, USA. [20]Department of Neurological Surgery, Feinberg Medical School, Northwestern University, Evanston, IL, USA. [21]Department of Chemistry, Northwestern University, Evanston, IL, USA. [22]Department of Electrical Engineering and Computer Science, Northwestern University, Evanston, IL, USA. [23]These authors contributed equally: Xinge Yu, Zhaoqian Xie, Yang Yu, Jungyup Lee. *e-mail: y-huang@northwestern.edu; jrogers@northwestern.edu

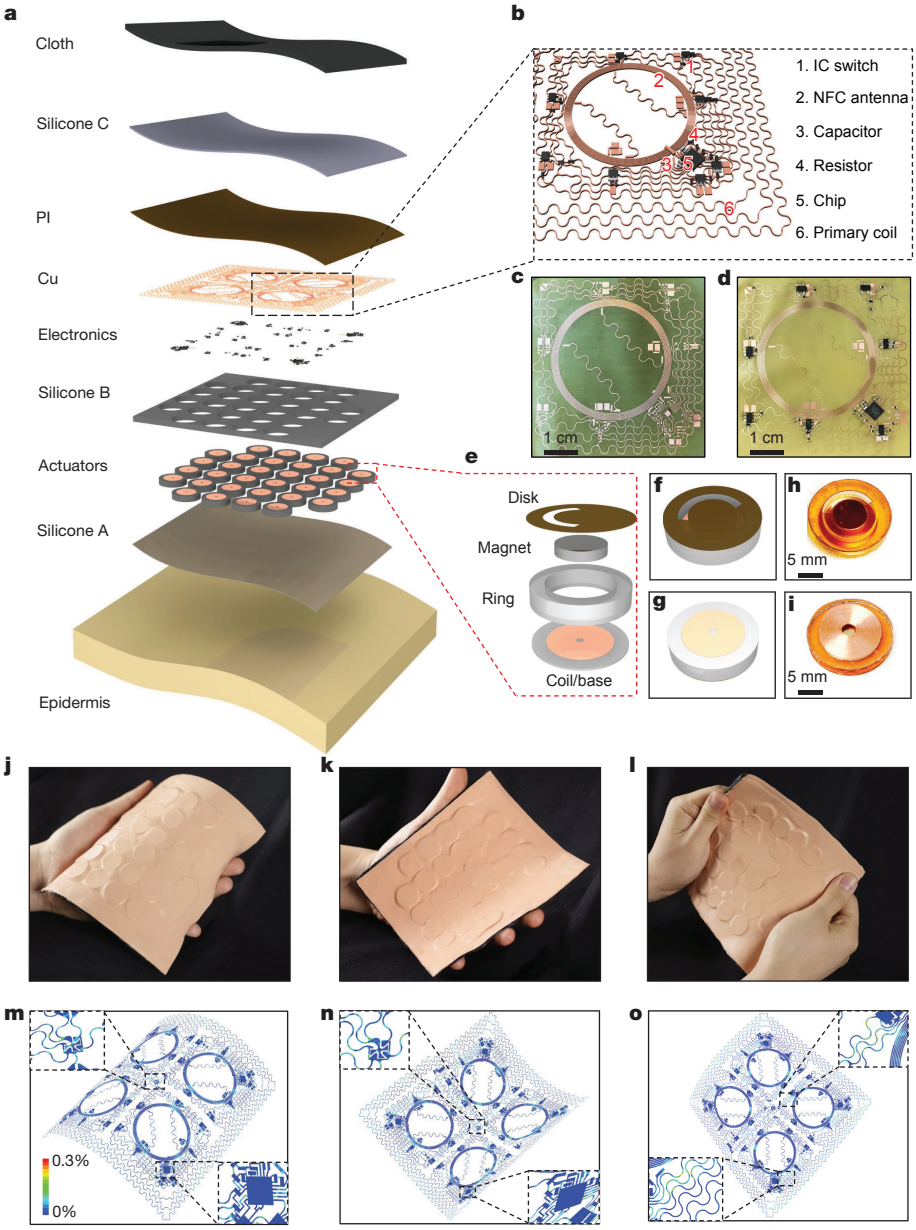

Fig. 1 | Design and architecture of an epidermal VR system. a, Exploded-view schematic illustration of a device with 32 independently controlled haptic actuators. **b**, Schematic illustration of the NFC electronics and circuit; the main circuit components are labelled 1–6. **c**, **d**, Optical images of an NFC coil before (**c**) and after (**d**) integrating the electronic components. **e**, Exploded-view schematic diagram of a haptic actuator. **f**, **g**, Schematic diagram of an actuator viewed from above (**f**) and below (**g**). **h**, **i**, Optical images of an actuator viewed from above (**h**) and below (**i**). **j**–**o**, Optical images (top row) and FEA results (bottom row) of an epidermal VR device under bending (**j**, **m**), folding (**k**, **n**) and twisting (**l**, **o**). The colour in **m**–**o** represents the equivalent strain, and the insets show the areas with relatively high strain levels. See Methods for details.

systems and power supplies[2,7]. As with related supporting hardware for electrotactile interfaces, the cumbersome nature of this type of technology and the limited ability to scale to monolithic, manufacturable platforms with large numbers of independently controlled actuators represent disadvantages that will hinder widespread adoption.

Here we introduce a set of materials, device designs, integration schemes and system layouts for wirelessly controlled and wirelessly powered, battery-free, haptic interfaces that incorporate large arrays of millimetre-scale vibratory actuators in soft, conformal sheets of electronics that laminate directly onto the skin in a simple, non-invasive and reversible manner. Multiple systems of this type, interfaced onto desired locations on the body with full, programmable control via a remote computer system, establish means to extend VR/AR experiences beyond visual and auditory sensations, with broad application possibilities. Figure 1a presents schematic illustrations of a representative platform, which we refer to as an epidermal VR interface. The construction takes the form of a multilayer stack that includes (1) a thin elastomeric layer as a reversible, soft, adhesive interface to the skin, (2) a silicone-encapsulated functional layer that supports a wireless control system, a means for receiving wirelessly transmitted power, and an interconnected array of actuators with associated drive electronics, and (3) a breathable, stretchable fabric coated with an thin film of silicone, as a physically tough but skin-conformal supporting substrate with strain-limiting mechanics to prevent damage to the functional materials and components. For aesthetics, a coating of silicone that incorporates skin-tone colouration and/or graphics can be included on the outward facing side of the fabric, or such features can be incorporated directly into the fabric itself. The electronics part of the functional layer consists of a collection of copper (Cu) traces encapsulated in polyimide (PI) and formed in narrow, filamentary serpentine geometries

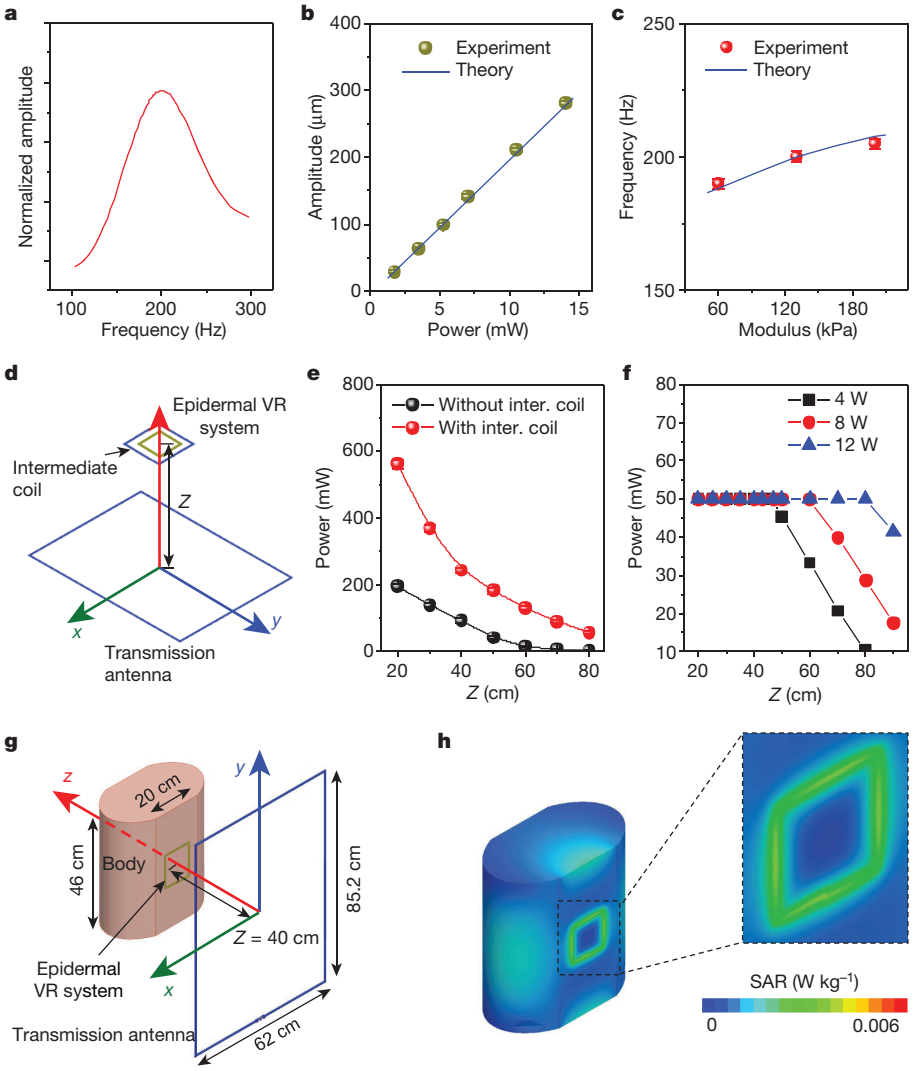

Fig. 2 | Optimized operation of key electrical and mechanical components of an epidermal VR system. a, Normalized amplitude–frequency response of a haptic actuator in contact with a skin phantom. **b**, Travel amplitude of the magnet as a function of the input power (data points) for an actuator in contact with skin phantoms with elastic moduli of 130 kPa. Here, and in **c**, the symbols and lines correspond to experimental and mechanics-simulated theoretical results, respectively. **c**, Dependence of the resonance frequency on the elastic modulus of the skin phantom (data points), over a range relevant for human skin. **d**, Schematic illustration of an epidermal VR device with an intermediate coil above a transmission antenna. **e**, Power harvested from the primary coil of an epidermal VR device with and without an integrated intermediate ('inter.') coil, as a function of distance in the *Z* direction. Here, and in **f**, the lines are guides to the eye. **f**, Power harvested from the primary coil of an epidermal VR device with an intermediate coil after power regulation, for various RF powers applied to the transmission antenna (4–12 W; see key). **g**, **h**, Schematic illustration of a representative epidermal VR system mounted on the body (**g**), and the SAR distribution (**h**). In **b**, **c**, **e**, **f**, error bars correspond to the calculated standard deviation.

according to quantitative design rules in stretchable electronics[9,10]. These traces interconnect a collection of small, chip-scale integrated circuit components and passive elements, including magnetic radio frequency (RF) loop antenna structures, resistors, capacitors, rectifiers and integrated circuit (IC) switches. System-on-a-chip (SoC) ICs that include microcontrollers with capabilities in near-field communication (NFC) and general input/output functionality (Fig. 1b–d) serve as control interfaces to a distributed set of mechanical vibratory actuators, referred to in the following as haptic actuators.

Supplementary Fig. 1e–i shows schematic diagrams and optical images of these actuators. Here, time-dependent Lorenz forces (Extended Data Fig. 1) follow from the passage of a time-varying current through a coil that surrounds a permanent magnet. The shell of the actuator consists of a ring-shaped elastomeric structure that provides space for the magnet to travel freely in the out-of-plane direction. A thin disk of PI mounted on top of the PDMS ring and laser-cut with a semicircular slit serves as a bonding location for the magnet. This construct forms a cantilever-like platform, capable of actuation via interactions between the magnet and current flowing through the coil at the base of the ring. These basic designs can, in principle, be extended to length scales that characterize the separation of mechanoreceptors in the skin of the arms, chest, back and legs (Supplementary Fig. 2). Moreover, miniaturization of this type of actuator by an order of magnitude increases the acceleration of the magnet during vibration by more than a factor of three for the same electrical power, such that the same contact pressure can be achieved by reducing the radial and thickness dimensions of the magnet by a factor of 10 and 3, respectively. As a result, further decreases in power consumption might be achievable by reducing the sizes of the actuators. (See details of scaling simulations in Methods.)

Careful optimization of the materials and designs of these actuators, guided by computational modelling, allows for power efficient operation as skin-coupled haptic interfaces. The diameter and thickness of the PI disk and the layout of the slit, the geometry of the PDMS ring,

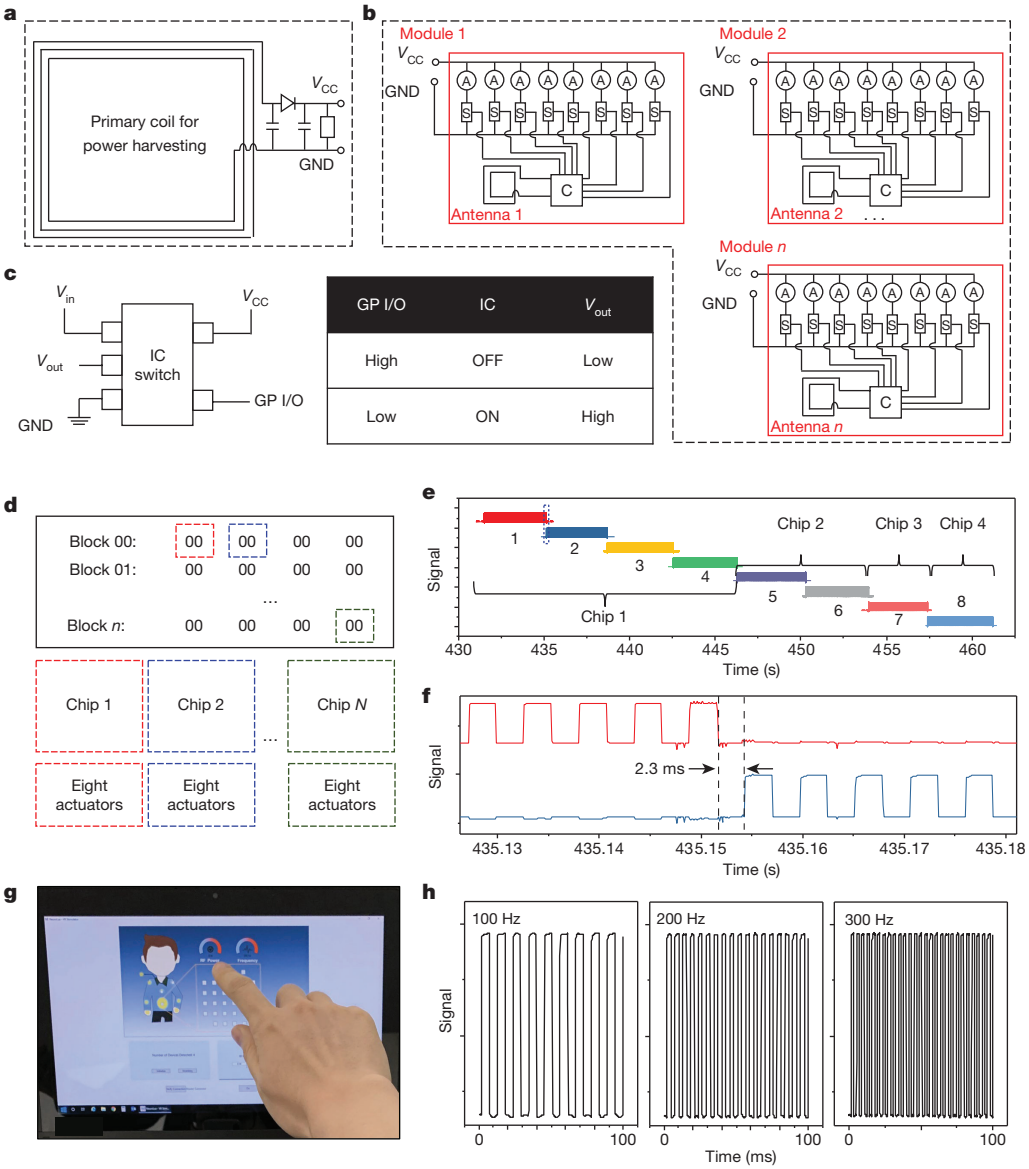

Fig. 3 | Wireless control strategies for epidermal VR systems. a, **b**, Circuit diagram for an epidermal VR device, including a large primary coil for power harvesting (**a**) and several control modules (**b**), each of which consists of a small antenna and an SoC, along with eight haptic actuators controlled by eight IC switches, independently. GND, ground; A, actuator; S, IC switch; C, SoC. **c**, Schematic diagram (left) and working principle (right) of an IC switch. The ON/OFF of the output voltage of the IC switch is controlled by GP I/O ports on the SoC. **d**, Diagram of the command interface that supports independent control over every actuator in the system. Each of the eight GP I/O ports in each SoC is defined by a one-byte command, such that $8 \times n$ actuators can be initiated in any form by a portfolio of n bytes. The dashed coloured boxes represent different SoCs. **e**, Response time of actuators controlled by four SoCs. The coloured plots represent different output signals of the actuators. **f**, A magnified view of the time required to switch from one actuator to another. **g**, Software interface of the control system. **h**, Three representative working frequencies for haptic actuators in an epidermal VR platform: 100 Hz, 200 Hz and 300 Hz.

the type and size of the magnet, and the configuration of the coil can be selected to satisfy requirements relevant to body-interfaced operation, across many mounting locations and body types, as outlined in quantitative detail in Extended Data Figs. 1–4. Frequencies in the range between 100 Hz and 300 Hz are of greatest interest because they provide the strongest sensations on human skin, owing to the intrinsic nature of the responses of the mechanoreceptors[11,12]. Here, amplitudes as small as several micrometres can yield distinct tactile responses[11]. Adjusting the angular extent of the slit in the PI disk presents a simple means to tune the resonant frequency of the actuator (Extended Data Figs. 2, 3) to a value of 200 Hz for operation on a skin phantom with an elastic modulus of 130 kPa. With optimized designs, these types of haptic actuators require only about 1.75 mW to induce a notable sensory responses on the fingertips and hands, with a corresponding amplitude of approximately 35 μm (Supplementary Videos 1, 2; Fig. 2b), without parasitic heating effects (Supplementary Fig. 3) and with the option of full system operation with small batteries. By comparison, widely used commercially available vibration actuators/motors (eccentric rotating mass actuators, linear resonant actuators and piezoelectric actuators) in consumer gadgets typically require >100 mW. Figure 2c and Extended Data Figs. 3, 4 summarize the dependence of the resonance frequency on the modulus of the phantom, from 60 kPa to 200 kPa. The results suggest a weak, almost negligible, variation in frequency over modulus values that span those characteristic of skin at different ages and across different regions of the body. The amplitude increases linearly with input power for all modulus values (Extended Data Figs. 3e, 4e). The motion of the actuator involves a vibrational deflection along the cantilever beam in a way that directly, and indirectly through inertial

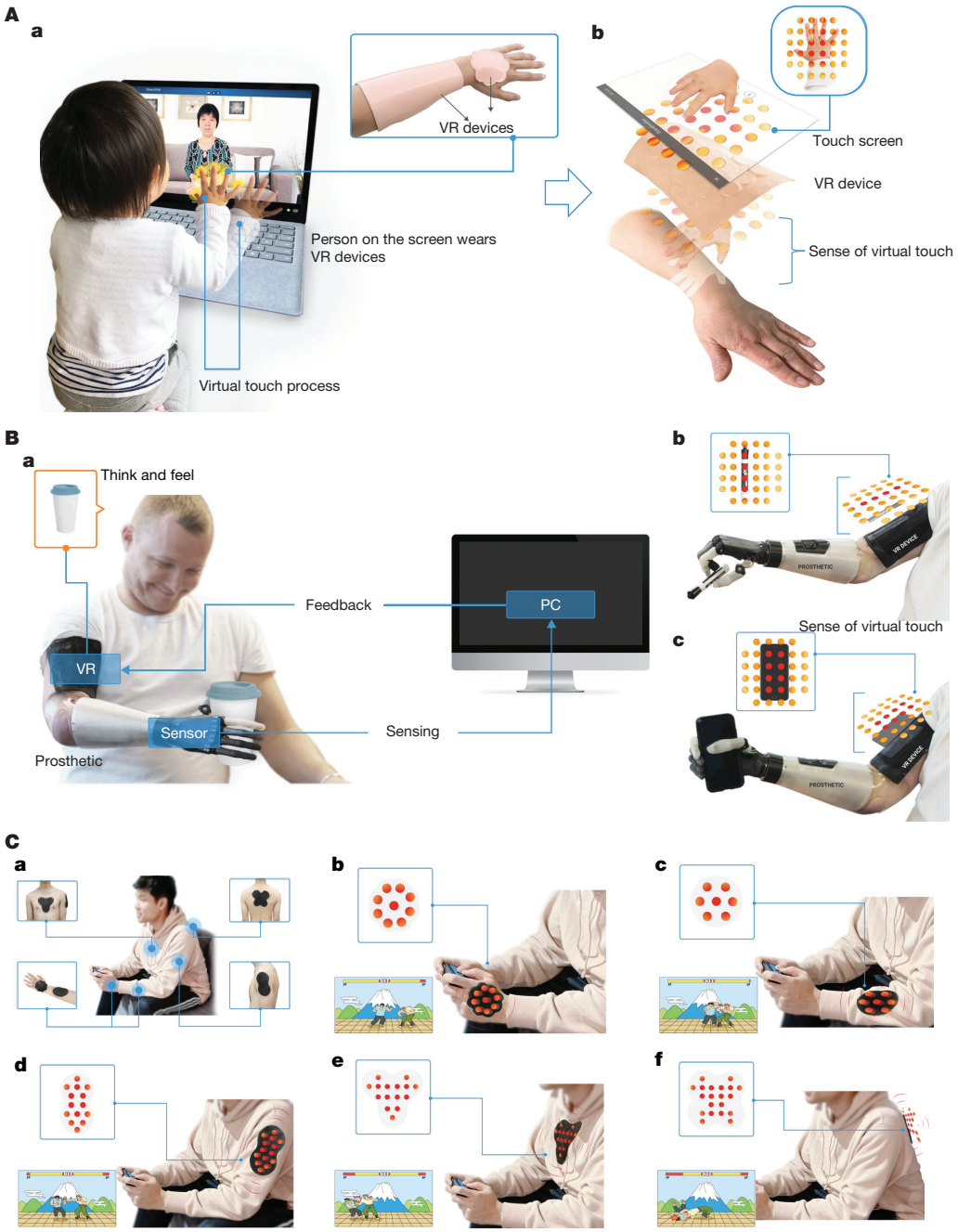

Fig. 4 | Examples of applications of epidermal VR systems. A, Social media application: **a**, a girl touches a screen that displays a video feed of her grandmother, who is wearing an epidermal VR device on her hand and her arm (inset photograph); **b**, a dynamic illustration of the pattern of 'virtual touch process' and 'sense of virtual touch'. **B**, Prosthetics application: **a**, a man with a lower-arm amputation wears a prosthetic arm with a robotic hand and an epidermal VR device on his upper arm; **b**, **c**, the device produces a haptic pattern of sensation ('think and feel') that reproduces the shape characteristics of objects ('feedback') held in the robotic hand ('sensing'). **C**, Gaming application: **a**, a man wears several epidermal VR devices on different parts of his body; **b**–**f**, devices activate when a strike occurs on the corresponding body part of the game character, namely, the hand (**b**), elbow (**c**), arm (**d**), chest (**e**) and back (**f**).

effects, couples to the skin. Careful optimization minimizes mechanical cross-talk between adjacent actuators (Extended Data Figs. 4f, 5).

These actuators connect to associated antenna structures and electronic components through conductive traces with designs that minimize strains and resistive losses and, at the same time, operate without failure under a full range of bending and twisting motions. As with actuator design, 3D finite-element analysis (FEA) techniques guide selection of the interconnect geometries and the overall system layouts (see Methods for details). The result is a soft, deformable platform capable of establishing a comfortable, non-irritating interface to the skin, across nearly any region of the body[13–15]. Computed distributions of strain in the copper and corresponding optical images in Fig. 1j–o show results for bending, folding and twisting. The equivalent strains remain below the elastic limit (0.3%) for a bend of about 145° (with a bending radius of approximately 5.1 cm), a fold of about 150° (folding radius approximately 5 cm) and a twist of about 50° (ref. [16]). (Fig. 1l shows a 'bend', Fig. 1k shows a 'fold'.) The overall shapes of the platforms can be designed to harmonize with anatomical features; examples include 'flower', 'oval', 'peanut', 'triangle' and 'butterfly' shapes (Supplementary Fig. 2).

NFC protocols serve as the basis for operation and coordinated control, with modes that are difficult or impossible to reproduce with battery-free far-field techniques[17]. Power delivery and data communication use different antennas, designed to allow independent operation without interference (Extended Data Fig. 6a, b)[18]. A large primary coil that exploits the full perimeter of the device platform harvests the power needed to operate the entire collection of actuators. Separate small antennas serve as wireless interfaces and power sources for each of the SoCs, each one of which supports independent control over eight actuators. Means for efficient harvesting and utilization of power are critical aspects of system design[18,19]. Most envisioned applications require wireless power transfer over distances of at least tens of centimetres, to allow integration of the RF power transmission antenna into the base of a chair, desk or bed[13]. As summarized in Extended Data Fig. 6c–i, the operating distance (Z) of a VR device (using a 12 cm × 12 cm square serpentine coil as the primary coil with a Q factor of 20, and 32 actuators all working at a set power of 1.75 mW) oriented parallel to the antenna is about 30 cm and 45 cm for transmission antennas with respective dimensions of 31.8 cm × 33.8 cm and 85.2 cm × 62.0 cm, and an input power of 12 W to the transmission antenna. The distance Z can be increased by increasing the power, optimizing the size of the transmission antenna and/or by decreasing the power consumption of the system by reducing the sizes of the actuators.

Addition of an intermediate, single-loop coil (20 × 20 cm; tuned to 13.56 MHz) incorporated directly into the device (Fig. 2d, Supplementary Fig. 4) further improves this range by locally increasing the strength of the magnetic field by a factor of about 10 (Extended Data Fig. 7). Figure 2d compares the power harvested by the primary coil as a function of position Z for cases with and without the intermediate coil, using a transmission antenna (85.2 cm × 62.0 cm) powered at 12 W. The intermediate coil increases the magnetic field strength by about 16 times for Z = 30 cm, and by about 11 times for Z = 50 cm. The corresponding increases in received power are approximately 2.5 times for Z = 30 cm, and 4.5 times for Z = 50 cm, influenced by the load (resistance) of the device[20]. The working range can reach 80 cm. An active power regulation system enabled by a linear voltage regulator ensures consistent operation throughout this full range of distances. Figure 2f highlights the ability to deliver a fixed output power from the primary coil of the device into a load resistor (2 kΩ) for operation of the transmission antenna at powers between 4 W and 12 W across a range of distances. The power output is stable for tilt angles up to 60° and after more than 10,000 cycles of bending to a radius of 2.8 cm (Extended Data Fig. 8, Supplementary Fig. 5). As shown in Fig. 2g, h and Supplementary Fig. 4, the mode of operation complies with guidelines outlined by the Federal Communications Commission (47 CFR Part 1.1310 and 15) and the Federal Drug Administration in terms of both the specific absorbed radiation (SAR) and the maximum permissible exposure (MPE). The maximum value of the SAR is 0.006 W kg^{-1} (Fig. 2h), substantially less than the exposure limit[21] of 0.08 W kg^{-1}. The maximum computed equivalent power density of electromagnetic fields is 0.8 mW cm^{-2} (Supplementary Fig. 6), which is below the MPE limit[21] of approximately 4.9 mW cm^{-2}.

The block diagram in Fig. 3a, b summarizes the system architecture and overall operation. The first part harvests power through a primary coil (Fig. 3a) via the transmission antenna. This power passes through a linear voltage regulator to provide a fixed, direct-current voltage (V_{CC}, where CC indicates common collector) to all of the haptic actuators. The second part provides control and communication via an array of interconnected SoCs, each with a separate small control antenna, and with operational control over eight haptic actuators through its general purpose input/output (GP I/O) ports (Fig. 3b). These ports generate square-wave signals by alternating the output of each GP I/O between its high and low settings, at programmable frequencies between 100 Hz and 300 Hz. An IC switch associated with each actuator (Fig. 3c) transforms V_{CC} into a square wave defined by the corresponding GP I/O, and this signal serves as input to the actuator. In this way, one SoC/IC switch combination allows for control/operation of eight actuators, simultaneously and independently. Scaling this architecture to include multiple unit cells of this type yields systems with arbitrarily large numbers of actuators, without limitation.

Wirelessly writing the necessary NFC Data Exchange Format (NDEF) messages into each SoC via the transmission antenna, which serves simultaneously as an RF reader, defines the output frequency to each haptic actuator, thus programming the entire system for operation. Unlike conventional multiplexing approaches to controlling actuators, a computer interfaced to the reader collects information on the identification codes for each of the SoCs in the system, thereby identifying every GP I/O port and haptic actuator. A one-byte message sets the ON/OFF command for each of the eight GP I/O ports on each SoC. All GP I/O ports are controlled independently. An entire system with 32 haptic actuators (4 SoCs, each with 8 GP I/Os) can be controlled in a single communication of four bytes—for example, a command of 'FF FF FF FF' sets all of the actuators to ON (Fig. 3d), and a command '01 00 00 00' sets to ON the actuator connected to the first GP I/O of the first SoC.

The time required to change from one system configuration to another is in the millisecond regime, as shown in Fig. 3e, f, which is about 50 times faster than the reaction time to tactile stimulation[22]. A graphical interface with a touch screen, as in Fig. 3g and Supplementary Fig. 7, allows a user to change patterns of actuation rapidly and, separately, to select the amplitudes and frequencies of the vibratory responses. An array of 32 lasers provides a means to visualize operation at the system level, via projection of individual beams reflected from each of the haptic actuators and onto a monitoring screen (Extended Data Figs. 9, 10 and Supplementary Video 3). Recordings from a high-speed camera replayed at 16.7× and 133× slow motion reveal the time dynamics of the vibratory motions of the actuators and their programmed control (Supplementary Video 4).

The transmission antennas and devices can be configured in various ways for different use scenarios (Supplementary Fig. 8). Replacing the IC switches with high-power compliance transistors and modifying the cantilever designs improves the power delivery to the actuators and increases their vibratory bandwidths and amplitudes, for enhanced sensation across different body types and anatomical locations. A single-stage voltage regulation scheme conditions the power-harvesting efficiencies of receiving antennas with different form factors. Figure 4A summarizes a possibility in virtual interactions via social media. Here, a girl virtually touches her grandmother's hand through an interface on the screen of a laptop that simultaneously displays a video/audio feed. In this example, two epidermal VR devices are mounted on the grandmother, who experiences a haptic sensation in the form of a continuous wave of vibratory excitation extending sequentially down from her forearm to her hand in a spatio-temporal pattern of touch to match that of the granddaughter's fingertips on the image on the touch screen. A second representative application is in tactile feedback for use of robotic prosthetic devices. Figure 4B shows a man, whose lower arm has been amputated, with an epidermal VR device on his residual limb as he uses a prosthetic arm to grasp objects. Here, sensors on the prosthetic detect the shape of the object and this information serves as input to create a virtual haptic representation of the shape on his upper arm. The third application is in haptic engagement in gaming. In the example of Fig. 4C, a gamer wears several epidermal VR devices across different locations of the body. As a strike occurs in this combat game, haptic actuation reproduces the pattern of the impact at a corresponding location.

The epidermal VR systems introduced here exploit thin, soft architectures capable of laminating directly onto the skin as a platform for programmable control of large arrays of miniaturized haptic actuators in wireless modes of operation and with lightweight, battery-free designs. This class of technology is qualitatively distinguished in form and function over previous attempts at programmable haptic interfaces

to the body. Comprehensive experimental and computational studies of the various subsystems in these platforms yield a basic understanding of their operation and a set of guidelines for design choices. Demonstrations in social media interactions, prosthetic feedback and video gaming are representative of a broad spectrum of potential applications, which also include systems for personalized rehabilitation, surgical training, educational feedback, and multimedia entertainment experiences. Many opportunities exist to improve the performance of these systems by increasing the strength of mechanical actuation at the skin interface.

Online content

Any methods, additional references, Nature Research reporting summaries, source data, extended data, supplementary information, acknowledgements, peer review information; details of author contributions and competing interests; and statements of data and code availability are available at https://doi.org/10.1038/s41586-019-1687-0.

1. Kapur, P., Jensen, M., Buxbaum, L. J., Jax, S. A. & Kuchenbecker, K. J. Spatially distributed tactile feedback for kinesthetic motion guidance. In *2010 IEEE Haptics Symp*. (ed. Basodogan, C.) 519–526 (IEEE, 2010).
2. Sardini, E., Serpelloni, M. & Pasqui, V. Wireless wearable T-shirt for posture monitoring during rehabilitation exercises. *IEEE Trans. Instrum. Meas.* **64**, 439–448 (2015).
3. Kim, Y. et al. A bioinspired flexible organic artificial afferent nerve. *Science* **360**, 998–1003 (2018).
4. Novich, S. D. & Eagleman, D. M. Using space and time to encode vibrotactile information: toward an estimate of the skin's achievable throughput. *Exp. Brain Res.* **233**, 2777–2788 (2015).
5. Sundaram, S. et al. Learning the signatures of the human grasp using a scalable tactile glove. *Nature* **569**, 698–702 (2019).
6. Withana, A., Groeger, D. & Steimle, R. Tacttoo: a thin and feel-through tattoo for on-skin tactile output. In *Proc. 31st Ann. ACM Symp. on User Interface Software and Technology* (ed. Wilson, A. D.) 365–378 (ACM, 2018).
7. Huang, C.-T., Shen, C.-L., Tang, C.-F. & Chang, S.-H. A wearable yarn-based piezo-resistive sensor. *Sens. Actuators A* **141**, 396–403 (2008).
8. Cogan, S. F. Neural stimulation and recording electrodes. *Annu. Rev. Biomed. Eng.* **10**, 275–309 (2008).
9. Song, Y. M. et al. Digital cameras with designs inspired by the arthropod eye. *Nature* **497**, 95–99 (2013).
10. Rogers, J. A., Someya, T. & Huang, Y. Materials and mechanics for stretchable electronics. *Science* **327**, 1603–1607 (2010).
11. Wilska, A. On the vibrational sensitivity in different regions of the body surface. *Acta Physiol. Scand.* **31**, 285–289 (1954).
12. Mahns, D. A., Perkins, N. M., Sahai, V., Robinson, L. & Rowe, M. J. Vibrotactile frequency discrimination in human hairy skin. *J. Neurophysiol.* **95**, 1442–1450 (2006).
13. Han, S. et al. Battery-free, wireless sensors for full-body pressure and temperature mapping. *Sci. Transl. Med.* **10**, eaan4950 (2018).
14. Kim, D.-H. et al. Epidermal electronics. *Science* **333**, 838–843 (2011).
15. Kim, J. et al. Battery-free, stretchable optoelectronic systems for wireless optical characterization of the skin. *Sci. Adv.* **2**, e1600418 (2016).
16. Zhang, Y. et al. Experimental and theoretical studies of serpentine microstructures bonded to prestrained elastomers for stretchable electronics. *Adv. Funct. Mater.* **24**, 2028–2037 (2014).
17. Huang, X. et al. Epidermal radio frequency electronics for wireless power transfer. *Microsyst. Nanoeng.* **2**, 16052 (2016).
18. Chung, H. U. et al. Binodal, wireless epidermal electronic systems with in-sensor analytics for neonatal intensive care. *Science* **363**, eaau0780 (2019).
19. Beh, T. C., Kato, M., Imura, T., Oh, S. & Hori, Y. Automated impedance matching system for robust wireless power transfer via magnetic resonance coupling. *IEEE Trans. Ind. Electron.* **60**, 3689–3698 (2013).
20. Kim, J., Son, H., Kim, K. & Park, Y. Efficiency analysis of magnetic resonance wireless power transfer with intermediate resonant coil. *IEEE Antennas Wirel. Propag. Lett.* **10**, 389–392 (2011).
21. The Electronic Code of Federal Regulations (e-CFR) Title 47, 1.1310. Radiofrequency radiation exposure limits. https://www.ecfr.gov/cgi-bin/retrieveECFR?gp=&SID=81a1c5a13f8d02f165a06af36937d612&mc=true&n=pt47.1.1&r=PART&ty=HTML#se47.1.1_11310 (e-CFR, 2019).
22. Akamatsu, M., Mackenzie, I. S. & Hasbroucq, T. A comparison of tactile, auditory, and visual feedback in a pointing task using a mouse-type device. *Ergonomics* **38**, 816–827 (1995).

Methods

Fabrication of the system of electronics

A sheet of polyimide (PI, 12.5 μm) coated with a thin layer of copper (Cu, 50–200 μm wide and 18 μm thick) served as the substrate for the antenna structures and the electrical interconnects. Photolithography and etching yielded patterns of Cu in the desired geometries. For systems smaller than 4 inches × 4 inches, the process used a positive photoresist (AZ P4620, AZ Electronic Materials) spin-cast at 3,000 r.p.m. for 30 s, soft baked on a hot plate at 110 °C for 4 min, exposed to ultraviolet (UV, wavelength 350–400 nm) light to a dose of 500 mJ cm^{-2}, and developed for ~70 s in a basic solution (AZ 400K/deionized (DI) water in a 1:3 volume ratio). For systems larger than 4 inches × 4 inches, the process used dry film photoresist (Dupont, 38 μm thick), bonded onto the Cu foil by a roll laminator at 110 °C, soft baked on a hot plate at 110 °C for 4 min, exposed to UV light to a dose of 500 mJ cm^{-2}, post baked on a hot plate at 110 °C for 2 min and developed for ~180 s in a basic solution (MIF 917/DI water in a 1:1 volume ratio), and wet etched (CE-100 copper etchant, Transene) for ~2 min with frequent rinsing with DI water. In both cases, the photoresist was removed by acetone and the substrates were then rinsed with DI water.

Fabrication of the haptic actuators

The first step involved placing a Cu coil (wire diameter of 50 μm, with 300 turns to form a coil with an inner diameter of 3 mm and an outer diameter of 14 mm (Yisu Electronics, Inc.)) in the centre of an acrylic mould (mould 1) with a silicone release reagent (Clearco Product Co., Inc.). Pouring a prepolymer to poly(dimethylsiloxane) (PDMS; Sylgard 184, Dow-Corning; 10:1 weight ratio of prepolymer to crosslinker) into mould 1 submerged the Cu coil under a layer of PDMS with modulus of ~1 MPa and thickness of 0.2 mm. Baking in an oven at 70 °C for 1 h cured the material into a solid, elastomeric form. Next, filling with additional PDMS prepolymer, and mounting in a second, matching mould (mould 2) held in place with set screws prepared the assembly for a second curing step (overnight in an oven at 70 °C) to seal the coil structure in PDMS (~1 MPa; inner and outer diameters of 18 mm and 12 mm, respectively; thickness of 2.5 mm), shaped to meet the design requirements. The dimensions of the resulting PDMS ring with coil in its base, formed by release from moulds 1 and 2, were: 2.4 mm in thickness and 18 mm in diameter, with an inner cavity of 2.2 mm depth and 12 mm diameter (Extended Data Fig. 2). The second part of the actuator consisted of a permanent magnet (nickel-plated neodymium magnet, diameter of 8 mm, thickness of 1.6 mm) mounted on a PI disk. Laser cutting formed circular shapes with diameters of 18 mm from sheets of PI (125 μm thick, DuPont) and semicircular slits with diameters of 8 mm and central angles of 217° (Extended Data Fig. 2). A strong double-sided adhesive (Kapton, DuPont) attached a disk-shaped magnet (nickel-coated neodymium magnet, diameter of 8 mm, thickness of 1.6 mm, weight 0.6 g, Bunting Magnetics Co.) on the cantilever part of the PI disk (18 mm diameter, 125 μm thick). The final step involved bonding the PI disk, with the magnet mounted on the back side, on top of the PDMS ring with a silicone adhesive (Kwik-Sil, WPI Inc.). Each completed actuator weighs 1.4 g. The frequency of the current input to the coil defined the frequency of vibration of the magnet. The magnitude of the current was controlled at a set point (~5 mA for experiments reported here).

Scaling simulation of the haptic actuators

Careful selection and optimization of various parameters of the actuators and the entire VR system focused partly on generating a sufficiently strong alternating magnetic field with the Cu coil to excite suitable vibrations of the magnet. According to the magnetic field distribution around the Cu coil[23], the acceleration a of the magnet can be expressed as

$$a \propto \frac{\sqrt{P_{\text{input}} SNn}\, D_{\text{outer}}^{1.5}}{\left(D_{\text{outer}}^2 + d^2\right)^{1.5}}$$

where P_{input} is the input power, S is the cross-sectional area of the copper wire, N is the layer number, n is the turn number of each layer, D_{outer} is the outer diameter of the Cu coil, and d is the distance between the Cu coil and the magnet (Extended Data Fig. 2). Further, the contact pressure p can be expressed as

$$p = a\rho h$$

where ρ and h are the mass density and the thickness of the cylindrical magnet, respectively. The pressure distribution on the skin associated with operation of the actuator can be calculated by FEA, as in Supplementary Fig. 9. These results suggest that the force f applied on the skin for an actuator with input power of 1.75 mW is 135 mN, from $f = \int_s p\,ds$. To examine the effects of miniaturization, we fix P_{input}, N and S, and reduce D_{outer} and d by 10 times. An example of miniaturization involves decreasing n by 10 times with S fixed. As a result, the acceleration of the magnet increases by ~3.6 times for the same power input, such that the same contact pressure can be achieved by reducing the radial and thickness dimensions of the magnet by a factor of 10 and 3, respectively. The size of other components in the actuator can be adjusted according to the size of the Cu coil.

Device integration and assembly

Low temperature solder joints bonded and electrically connected all of the components, including the SoCs (RF430FRL15xH NFC, Texas Instruments), jumper wires (resistors, 0 Ω, Stackpole Electronics, Inc.), capacitors (10 nF to 2.2 μF, Murata Electronics North America), diodes (SMP1345, Skyworks Solutions, Inc.), power regulator (L78L, STMicroelectronics), IC switches (74LVC1G384, Nexperia BV), jump wires and haptic actuators to corresponding contact pads on the Cu/PI substrate. A thin (~0.2 mm) coating of an ultra-low-modulus silicone material (0.1 mm Silicone C, Silbione, ~3.0 kPa, Ilkem Silicones) on a stretchable fabric substrate (Spandex) served as an adhesive between the cloth and the electronic/haptic platform. Casting and curing a low modulus formulation of PDMS (Silicone B, PDMS, ~60 kPa, Sylgard 184, Dow-Corning) formed a uniform encapsulation layer (2.5 mm thick) over the electrical connections. A layer of skin-coloured PDMS (Silicone A, PDMS, ~0.2 mm, ~60 kPa, Sylgard 184, Dow-Corning) aligned and bonded on top of the device acted as the top encapsulation layer. These soft silicone coatings provided reversible adhesion to the skin, with an adhesion energy of ~90 N m^{-1} for hairless areas and ~80 N m^{-1} for hairy areas (Supplementary Fig. 10). Thin PI (12.5 μm) layers with the same dimensions as the cantilever beams in the haptic actuators were aligned and placed on top of the actuators before covering the top encapsulation layer, enabling the magnets to have freedom for vibratory motions. The total weight is 130 g for a system with 32 actuators in a square array, 40 g for the flower shaped device, 38 g for the oval shaped device, 81 g for the peanut shaped device, 99 g for the triangle shaped device and 120 g for the butterfly shaped device. Supplementary Fig. 11 shows that the water vapour transmission rate (WVTR) of the silicone/fabric sample is ~0.55 g h^{-1} m^{-2}. The WVTR of a similar sample, but with perforating holes (1 mm diameter and 8 mm pitch in a square lattice, with a hole area fraction α of ~1.2%) is ~3.69 g h^{-1} m^{-2}, which is comparable to that of a conventional breathable waterproof bandage (5.72 g h^{-1} m^{-2}) and somewhat smaller than that of a standard cloth bandage g (9.15 g h^{-1} m^{-2}) (Mannings, Hong Kong). We estimate that the complete epidermal VR device, with all of the impermeable active components and interconnects, can accommodate perforations at an overall areal density of $\alpha = 1.2\%$, comparable to that of the test structure. As a result, the WVTR for a system with perforations at this density should also be in the range of 3–4 g h^{-1} m^{-2}. These epidermal VR devices can be worn on the skin (including hairy areas) for extended periods, with various levels of physical activity, without irritation (Supplementary Fig. 12).

Mechanics simulation of the epidermal VR device

The commercial software ABAQUS (v6.10) was used to study the mechanics of the devices. The layouts of the chips and the shapes of the interconnects were optimized to decrease the strain/stress level and to avoid entanglements in the interconnects under different types of external loads (bending, folding and twisting) (Fig. 1m–o). The resonance frequency of the actuator was tuned to 200 Hz (the frequency to which humans are most sensitive) by designing the central angle θ of the PI layer in the actuator (Fig. 1e, Extended Data Fig. 2) to increase the vibration intensity. The arrangement of the actuators was optimized to decrease the mutual interference between them by adjusting their relative angles (Extended Data Fig. 5). The fabric cloth, Silicone A, Silicone B and Silicone C, PDMS, phantom skin and magnet were modelled by hexahedron elements (C3D8R) while the thin copper and PI film were modelled by composite shell elements (S4R). The number of elements in the model was ~3×10^7, and the minimal element size was 1/6 of the width of the narrowest interconnects (50 μm). The mesh convergence of the simulation was guaranteed for all cases. The elastic modulus (E), Poisson's ratio (v) and density (ρ) are as follows: $E_{cloth} = 391$ kPa, $v_{cloth} = 0.4$, $\rho_{cloth} = 0.96 \times 10^3$ kg m^{-3}; $E_{Silicone\_A} = 60$ kPa, $v_{Silicone\_A} = 0.5$, $\rho_{Silicone\_A} = 0.96 \times 10^3$ kg m^{-3}; $E_{Silicone\_B} = 60$ kPa, $v_{Silicone\_B} = 0.5$, $\rho_{Silicone\_B} = 0.96 \times 10^3$ kg m^{-3}; $E_{Silicone\_C} = 3$ kPa, $v_{Silicone\_C} = 0.5$, $\rho_{Silicone\_C} = 0.96 \times 10^3$ kg m^{-3}; $E_{PDMS} = 1$ MPa, $v_{PDMS} = 0.5$, $\rho_{PDMS} = 0.96 \times 10^3$ kg m^{-3}; $E_{skin} = 130$ kPa, $v_{skin} = 0.5$, $\rho_{skin} = 1.05 \times 10^3$ kg m^{-3}; $E_{magnet} = 113$ GPa, $v_{magnet} = 0.34$, $\rho_{magnet} = 8.08 \times 10^3$ kg m^{-3}; $E_{PI} = 2.5$ GPa, $v_{PI} = 0.34$, $\rho_{PI} = 0.91 \times 10^3$ kg m^{-3}; and $E_{Cu} = 119$ GPa, $v_{Cu} = 0.32$, $\rho_{Cu} = 8.96 \times 10^3$ kg m^{-3}.

Electromagnetic simulation of the epidermal VR device

The finite-element method was used in the electromagnetic simulations to study the magnetic field around the transmission antenna, primary coil, NFC coil, Cu coil (in actuators) and intermediate coil. The simulations were performed using commercial software Ansys HFSS 15 (Ansys Inc.), where the lumped port was used, and the port impedance was set according to the matching capacitor (see below). An adaptive mesh (tetrahedron elements), together with a spherical surface (2,000 mm in radius) as the radiation boundary, were adopted to ensure computational accuracy. The electromagnetic parameters in the material library of Ansys HFSS were used in the simulation.

Characterization of the intermediate coil

The resistance R and inductance L of an intermediate coil (using copper wire 0.7 mm in diameter) with dimensions 20 cm × 20 cm were measured with an impedance analyser. The results agree with simulations (Extended Data Fig. 7e, f). Addition of a matching capacitor with $C = 168$ pF yields a resonant frequency f of ~13.56 MHz (using $f = 1/[2\pi(LC)^{0.5}]$). The Q factor of the intermediate coil, defined by $Q = 2\pi fL/R$, is ~200 at a frequency of 13.56 MHz (Extended Data Fig. 7g).

Electromagnetic simulations for SAR and MPE

The system utilizes RF at 13.56 MHz, a frequency where biological tissues exhibit negligible absorption. The position of the body, therefore, has little effect on the operation, and the system functions well with a variety of obstacles in the environment, even including metal features, owing to the magnetic nature of the wireless link. FEA (using Ansys HFSS 15) was used to determine whether the epidermal VR platform operates within the specific absorbed radiation (SAR) and maximum permissible exposure (MPE) requirements outlined by the Federal Communications Commission (FCC) CFR Part 1.1310. The maximum transmitting power (12 W) of the transmission antenna (852 mm × 620 mm) was adopted in the simulation. The impedance of the circuit part is equivalent to a 170-Ω (the minimal load of the VR system) resistor, measured in the experiments, in series with the primary coil. The distance between the body and the coils/antennas of the epidermal VR system is 3 mm, which is the distance when the epidermal VR system is mounted on the body. The density of the body is taken as 1,000 kg m^{-3}.

NFC protocols, software control and system operation

Programming each SoC (RF430FRL15xH, Texas Instruments) with the Code Composer Studio (CCS) enabled the generation of square wave signals by alternating the output of the GP I/O port between its HIGH (high voltage output) and LOW (zero voltage output) settings. The frequency of the resulting square waves can be adjusted from 100 Hz to 300 Hz in a user-definable way through the software interface through changes in the SoC program. Each SoC controls eight separate GP I/O ports, and each of these can be controlled independently. The program incorporated an interrupt mechanism as the control on and off for the square wave. Writing a specific hexadecimal value into a particular register on the SoC activated the GP I/O port to generate the square wave signal. Writing any other hexadecimal value into this same register deactivated the port. As such, the interrupt acts as the control mechanism for the square wave. Other hexadecimal commands initiated data transfer via NFC Data Exchange Format (NDEF) messages. The necessary NDEF messages can be written into the SoC with a transmission antenna that operates at 13.56 MHz (FEIG, ID ISC. LRM2500-A), with an output power between 1 W and 12 W and the ability to interface to a computer/laptop via a USB port. The reader, connected to a computer/laptop, in this manner served as an interface to control the writing process using a custom graphical user interface. The software interface displays the connection status of the reader with the computer. Each virtual button (pixel) on the touch panel is associated with a 4-byte command. Control of each actuator can, in this way, be achieved without any interference or cross-talk. To avoid time delay, sequential operation was programmed into the SoC, leading to millisecond response times. SoCs can be differentiated from one another by their unique ID numbers (Supplementary Fig. 5). In this way, control of multiple SoCs can be accomplished without uncertainties in directionality in RF transmission.

Visualization of system level operation using an array of 32 lasers

The measurements relied on a custom-built system with an array of 32 lasers. Each laser beam (635 nm, 2 mW continuous wave) reflects from a small reflective disk (0.15-mm-thick pieces of glass of diameter 8 mm, coated with 10 nm Cr and 100 nm Au) mounted on a corresponding haptic actuator in the epidermal VR system. The full collection of reflected beams projects onto a monitoring screen to allow direct visualization of the spatial patterns of activation, as well as the amplitudes and orientations of the vibratory motions of the cantilevers associated with the actuators. The long light path geometrically converts the small amplitude vibrations of the actuators into large motions of the reflected spots, for easy visualization. An optical system of mounting stages allowed adjustment of each laser beam, including its incident angle, tilt angle and distance from the actuators. Each of the 32 laser modules was held by an angle post clamp, enabling an independently adjustable laser pattern to be configured. Once a laser module was adjusted to the proper position, the angle post clamps were fixed.

In this customized system, six horizontal posts supported the 32 laser modules: two of the posts supported four modules, the rest each supported six modules. The six posts were arranged one above the other, and this array was mounted on two vertical posts by angle post clamps. The two vertical posts were fixed on a solid aluminium optical breadboard (Extended Data Fig. 9a). Careful adjustments yielded a pattern of laser beams that were aligned with all the haptic actuators across the device.

Reporting summary

Further information on research design is available in the Nature Research Reporting Summary linked to this paper.

Data availability

All data are contained within the manuscript. Raw data are available from the corresponding authors upon reasonable request.

Code availability

Custom code used in this study is available from the corresponding authors upon reasonable request.

23. Lee, Y. *RFID Coil Design* (Microchip Technology Inc., 1998).

Acknowledgements We gratefully acknolwedge C. J. Su, T. Banks, J. H. Kim, Y. G. Xue and J. K. Chang for their efforts in constructing and testing the optimized systems. This work was supported by the Center for Bio-Integrated Electronics at Northwestern University. Z.X. and X.F. acknowledge support from the National Basic Research Program of China (grant number 2015CB351900) and the National Natural Science Foundation of China (grant numbers 11320101001 and 11402134). X.Y., Z.X., D.L. and Y.L. acknowledge support from the City University of Hong Kong (grant number 9610423). R.S. acknowledges support from the Engineering and Physical Sciences Research Council (grant number EP/L016028/1) and the China Scholarship Council. Y.H. acknowledges support from the NSF (grant number 1635443).

Author contributions X.Y., Z.X., Y.Y. and J.L. contributed equally to this work. X.Y, Z.X., H.Y. and J.A.R. conceived the ideas, designed the experiments and wrote the manuscript. X.Y., Z.X., J.L., J.R., A.V., H.L., X.N., A.A., D.L., B.J., R.S., Y.L., J.C., Q.H., C.L., S.K., P.G., C.Z., Y.Z., Y.X., Q.G., A.C., P.T., W.L., J.J., Y.Y., J.C., C.T., B.K., K.L., X.F. and J.C. performed experiments and analysed the experimental data. Z.X. led the structural designs and performed electromagnetic and mechanical modelling, with assistance from B.J., Q.H., C.Z. and Y.X.

Competing interests The authors declare no competing interests.

Additional information
Supplementary information is available for this paper at https://doi.org/10.1038/s41586-019-1687-0.
Correspondence and requests for materials should be addressed to Y.H. or J.A.R.
Peer review information *Nature* thanks Sriram Subramanian, Xiaoming Tao and the other, anonymous, reviewer(s) for their contribution to the peer review of this work.
Reprints and permissions information is available at http://www.nature.com/reprints.

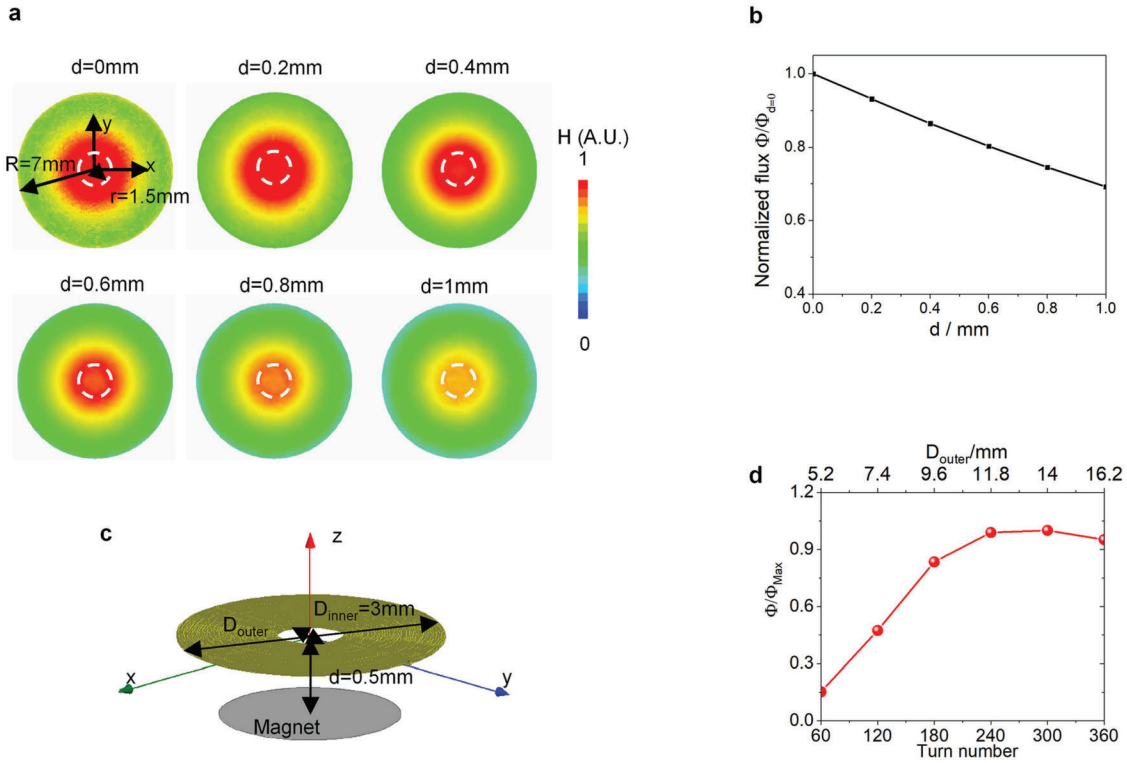

Extended Data Fig. 1 | Study of the magnetic field strength in an actuator. a, Distribution of the normalized magnetic field strength (H) around the Cu coil (300 turns) used in the actuator, where d is the distance between the Cu coil and the magnet. The dashed white circles correspond to the holes in the Cu coil. **b**, Normalized magnetic flux ($\Phi/\Phi_{d=0}$) through the haptic actuator versus the distance to the Cu coil (300 turns) of the actuator. **c**, Schematic illustration of the distance between a haptic actuator and a Cu coil in the actuator. **d**, The normalized magnetic flux (Φ/Φ_{Max}) through the magnet versus turn number and outer diameter (D_{outer}) of the Cu coil.

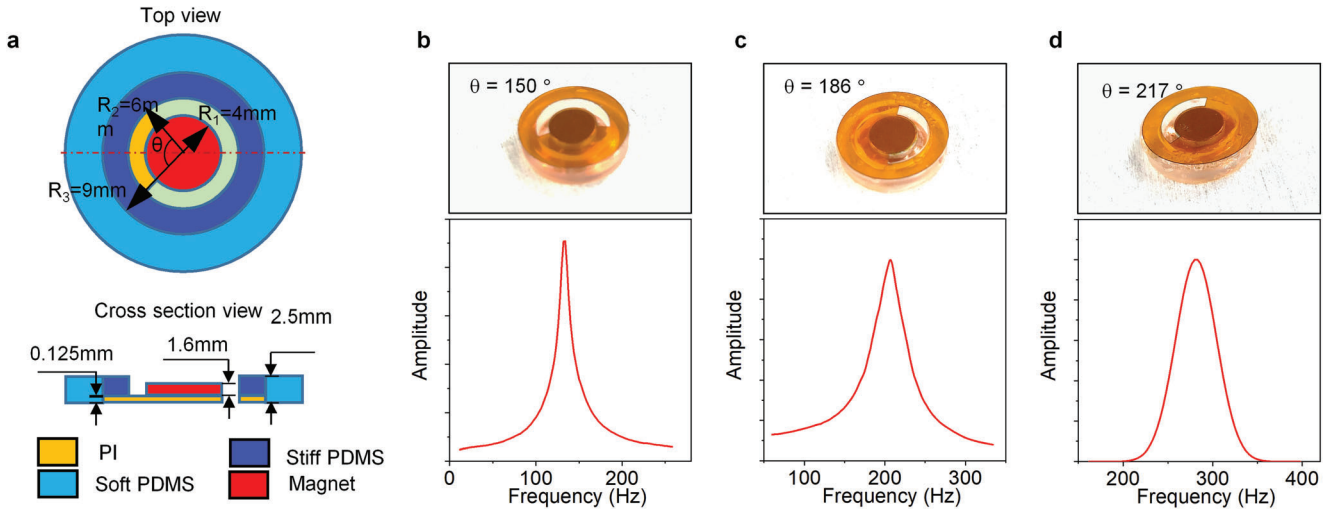

Extended Data Fig. 2 | Resonant frequency tuning of the actuator. a, Top view and cross-sectional view of the actuator design. The parameters presented here are optimized for tuning the resonance frequency to the skin-sensitive range. **b**–**d**, Optical images and normalized amplitude–frequency curves of three actuators with different central angles (θ) of 150° (**b**), 186° (**c**) and 217° (**d**), working without any contact. The actuators shown in **b** and **c** are 18 mm in diameter and 2.5 mm thick.

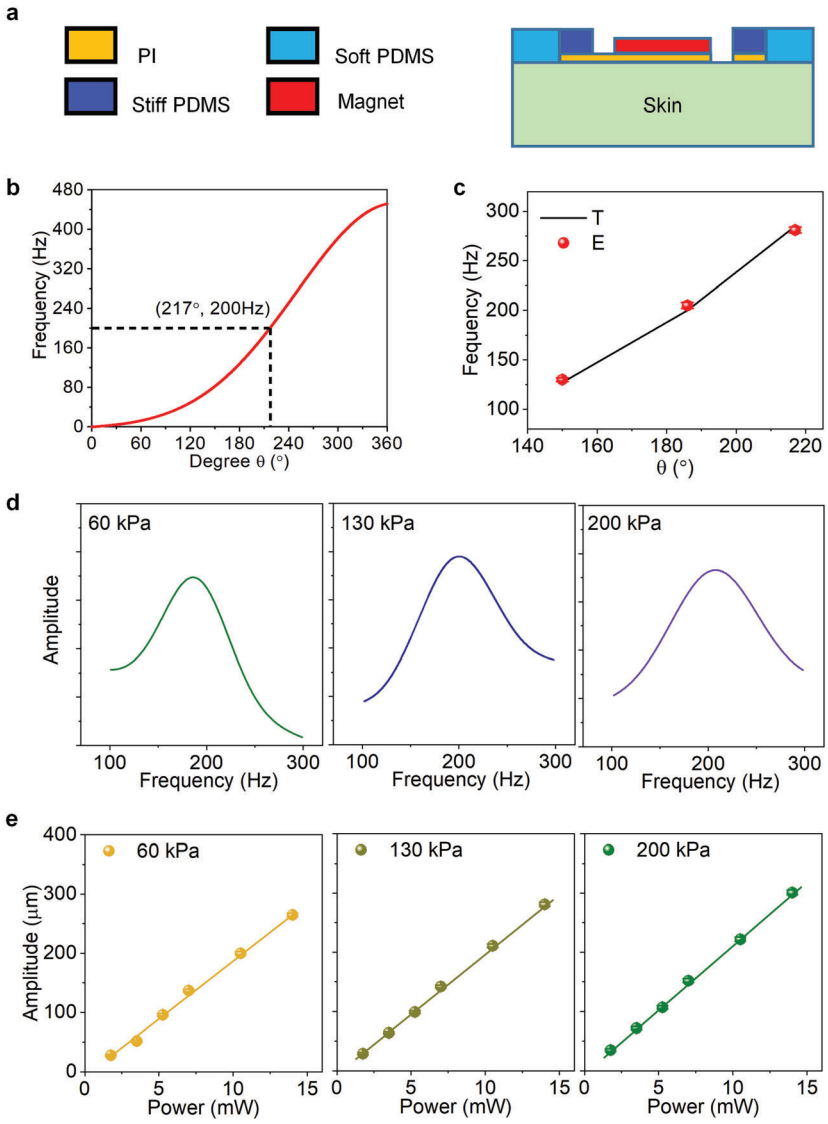

Extended Data Fig. 3 | Optimization of the actuator. a, Cross-sectional schematic illustration of an actuator in contact with skin. **b**, Theoretical results of the resonance frequency of actuators shown in **a** versus the central angle θ of the PI handling layer. The dashed lines indicate the resonance frequency of 200 Hz at $\theta = 217°$. **c**, Comparison of experimental (E; data symbols) and simulation (theory, T; lines) results. **d**, Experimental results of the normalized amplitude–frequency curves of the actuator ($\theta = 217°$) in contact with skin, for different values of skin elastic modulus: 60 kPa, 130 kPa and 200 kPa. **e**, Travel amplitude of the magnet as a function of the input power (data points) for an actuator in contact with artificial skin samples with elastic moduli of 60 kPa, 130 kPa and 200 kPa. In **c**, **e**, error bars correspond to the calculated standard deviation.

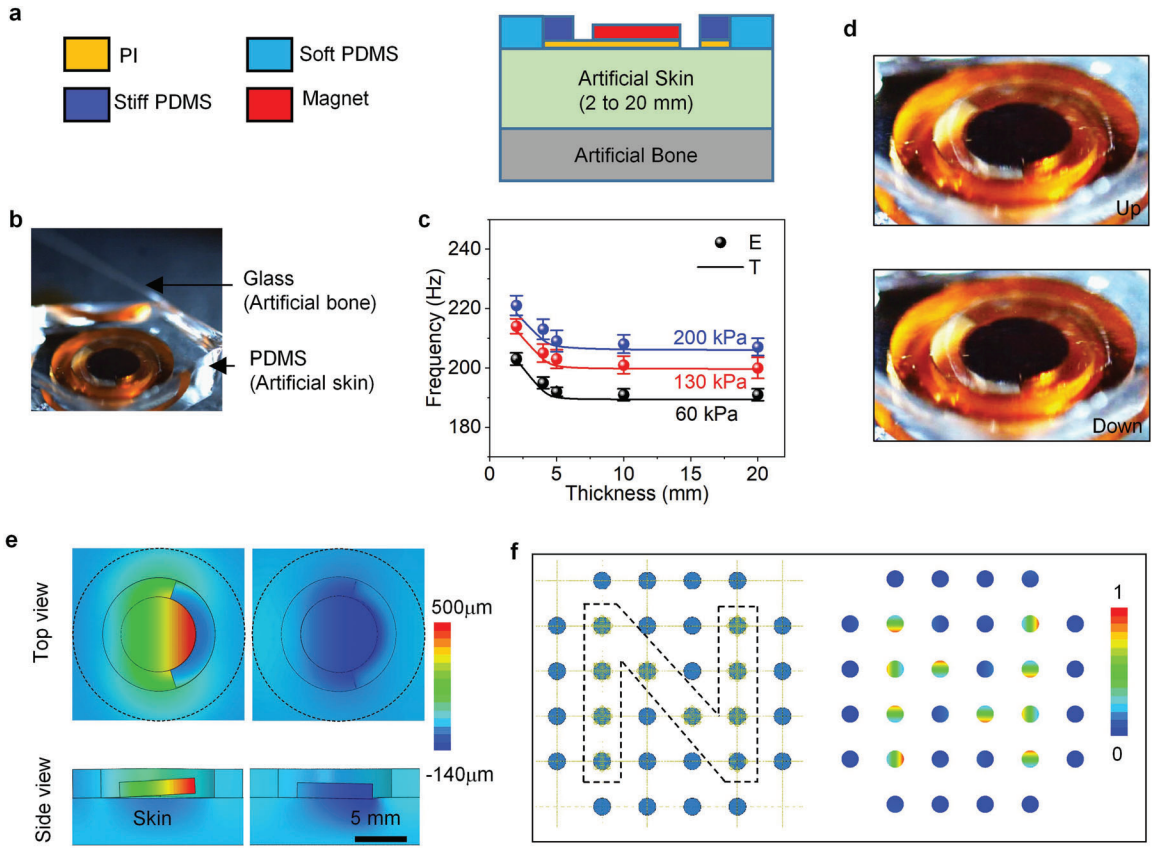

Extended Data Fig. 4 | Study of the mechanical behaviour of the actuator when in contact with skin. a, **b**, Cross-sectional schematic illustration (**a**) and optical image (**b**) of an actuator in contact with artificial skin. Here PDMS, serving as artificial skin, had three different values of elastic modulus, and glass was used for artificial bone. **c**, Comparison of the experimental (E) and simulation (theory, T) results of the resonance frequency of the actuator in contact with different moduli and thicknesses of artificial skin. The error bars correspond to the calculated standard deviation. **d**, Optical images captured using a high-speed camera and a working actuator travelling up and down, when in contact with 130-kPa artificial skin. **e**, FEA results for the amplitude of an actuator: left, when separated from skin; right, when in contact with skin. **f**, Schematic illustration and FEA results (colour-coded amplitude) for mechanical coupling between an array of haptic actuators, with activation in an 'N' pattern.

a

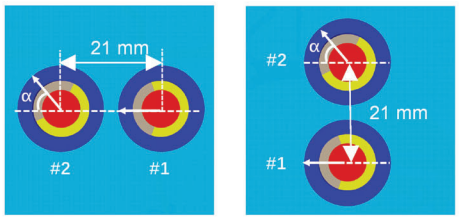

α (°)	Amplitude ratio
0	5.9%
45	2.8%
90	5.9%
135	8.0%
180	7.5%
225	8.0%
270	5.9%
315	2.8%

α (°)	Amplitude ratio
0	9.9%
45	5.8%
90	3.3%
135	9.4%
180	15.1%
225	11.3%
270	5.7%
315	7.4%

b

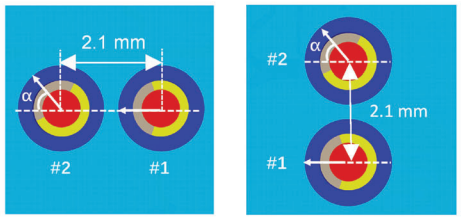

α (°)	Amplitude ratio
0	3.7 %
45	1.2 %
90	3.9 %
135	5.4 %
180	4.6 %
225	5.4 %
270	3.9 %
315	1.2 %

α (°)	Amplitude ratio
0	6.3 %
45	3.4 %
90	1.1 %
135	3.6 %
180	6.6 %
225	4.2 %
270	1.3 %
315	5.2 %

c

α=0°

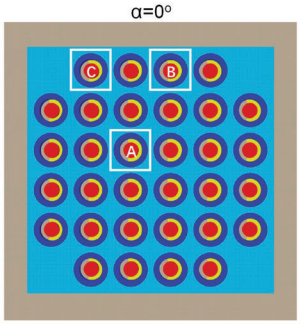

	0.03	0.03	0.04	0.03	
0.02	0.02	0.15	0.02	0.03	0.03
0.01	0.01	1.00	0.01	0.02	0.02
0.02	0.02	0.14	0.02	0.02	0.02
0.02	0.02	0.02	0.03	0.02	0.02
	0.02	0.02	0.02	0.02	

	0.01	0.01	1.00	0.02	
0.03	0.03	0.02	0.14	0.02	0.03
0.03	0.03	0.04	0.03	0.03	0.03
0.02	0.02	0.02	0.02	0.02	0.01
0.01	0.01	0.01	0.00	0.00	0.01
	0.02	0.02	0.02	0.02	

	1.00	0.01	0.01	0.02	
0.01	0.13	0.02	0.03	0.03	0.03
0.02	0.02	0.03	0.03	0.03	0.03
0.01	0.02	0.02	0.01	0.01	0.01
0.01	0.01	0.01	0.01	0.01	0.01
	0.02	0.02	0.02	0.01	

α=45°

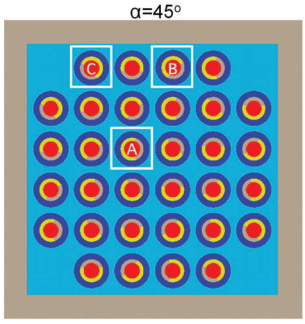

	0.03	0.01	0.04	0.03	
0.02	0.02	0.06	0.03	0.02	0.02
0.01	0.02	1.00	0.03	0.01	0.03
0.02	0.02	0.06	0.01	0.03	0.03
0.03	0.02	0.01	0.03	0.03	0.02
	0.01	0.02	0.03	0.01	

	0.03	0.05	1.00	0.01	
0.04	0.03	0.05	0.06	0.03	0.03
0.03	0.02	0.04	0.04	0.02	0.05
0.02	0.02	0.03	0.01	0.03	0.02
0.01	0.02	0.02	0.01	0.01	0.02
	0.02	0.02	0.02	0.02	

	1.00	0.06	0.03	0.03	
0.01	0.01	0.02	0.03	0.02	0.02
0.02	0.01	0.03	0.03	0.01	0.03
0.02	0.01	0.03	0.01	0.01	0.01
0.01	0.02	0.02	0.01	0.01	0.02
	0.01	0.02	0.02	0.02	

α=90°/270°

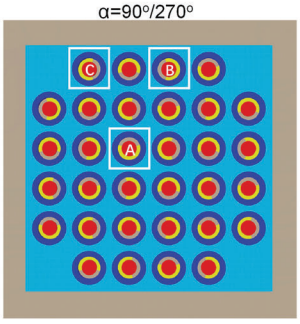

	0.01	0.02	0.01	0.03	
0.01	0.04	0.05	0.03	0.02	0.03
0.04	0.03	1.00	0.03	0.04	0.01
0.02	0.03	0.04	0.04	0.02	0.01
0.04	0.01	0.03	0.01	0.04	0.01
	0.03	0.01	0.03	0.02	

	0.01	0.06	1.00	0.04	
0.02	0.02	0.03	0.06	0.01	0.01
0.02	0.03	0.02	0.04	0.01	0.03
0.02	0.03	0.03	0.01	0.03	0.02
0.03	0.01	0.02	0.01	0.01	0.01
	0.02	0.01	0.00	0.00	

	1.00	0.04	0.01	0.01	
0.01	0.01	0.01	0.01	0.03	0.02
0.01	0.03	0.01	0.03	0.02	0.03
0.02	0.02	0.03	0.01	0.03	0.03
0.01	0.01	0.01	0.01	0.02	0.01
	0.01	0.00	0.01	0.01	

Extended Data Fig. 5 | See next page for caption.

Extended Data Fig. 5 | Mutual interference study of an actuator array. a, Mutual interference of two actuators at different relative angles α at 200 Hz. Two representative cases were studied, with one actuator (no. 1) positioned along (left) or perpendicular to (right) the bisector of the other actuator (no. 2). Here, only actuator 1 was actuated. The amplitude ratio, that is, the amplitude of actuator 2 over the amplitude (induced by mutual interference) of actuator 1, shown in the table demonstrates that $\alpha = 45°$, 90° and 270° result in relatively small mutual interference for both representative cases simultaneously. **b**, Mutual interference of two small actuators at different relative angles α at their resonant frequency of 200 Hz. The size of the actuators and the distance between them were scaled to 1/10 of the original design as shown in **a**, that is, the distance between two actuators was 2.1 mm rather than 21 mm. Here the thickness of the PI disk was set at 1.8 μm to enable the resonant frequency for the small actuator to be 200 Hz. Two representative cases were studied, with one actuator (no. 1) positioned along (left) or perpendicular to (right) the bisector of the other actuator (no. 2). Here only actuator 1 was actuated. The amplitude ratios (actuator 2 to actuator 1) due to mutual interference are shown in the table. **c**, Optimization of the actuators' arrangement. The mutual interference among actuators was studied for $\alpha = 0°$, $\alpha = 45°$ and a combination of 90°/270° referring to the simulation results in **a**, and for representative cases when actuators A (around the centre), B (near the boundary) and C (near the corner) are actuated separately. The results show that $\alpha = 90°/270°$ yields the smallest mutual interference (see tables under). The number gives the amplitude ratio due to the mutual interference among the actuators—that is, the amplitude of all actuators over the amplitude of the activated actuator—where 1 represents the activated actuator.

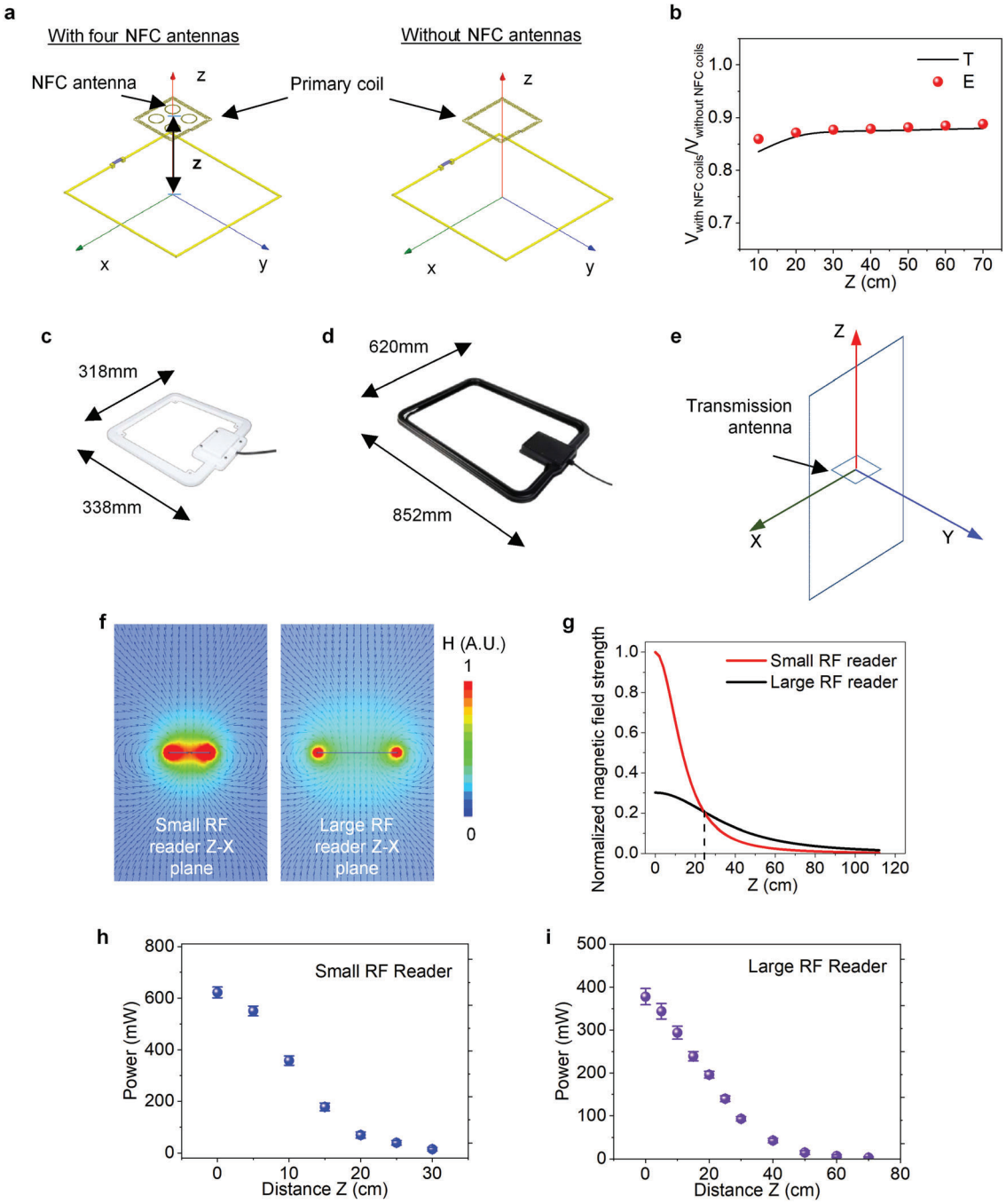

Extended Data Fig. 6 | Study of the key electrical components of the epidermal VR system. a, Interference between the primary coil and NFC antennas. Shown are schematic illustrations of a primary coil with (left) or without (right) four NFC antennas along the *Z* direction of the transmission antenna. **b**, Comparison of experimental (E) and theoretical (T) results of voltage induced by a single primary coil versus a primary coil with four NFC antennas. **c**, **d**, Transmission antennas used for operating the VR devices: **c**, small size, 318 mm × 338 mm; and **d**, large size, 620 mm × 852 mm. **e**, An transmission antenna placed in the *X*–*Y* plane. **f**, The magnetic field strength (*H*) in the *Z*–*X* plane (the middle plane of the coil) for the small (left) and large (right) transmission antennas (RF readers). **g**, Theoretical results show that the small and large transmission antennas are suitable for short (<24 cm) and long (>24 cm) working distances, respectively. **h**, **i**, Output power of the serpentine primary coil of the epidermal VR device as a function of distance to the small transmission antenna (**h**), and the large transmission antenna (**i**). The error bars correspond to the calculated standard deviation.

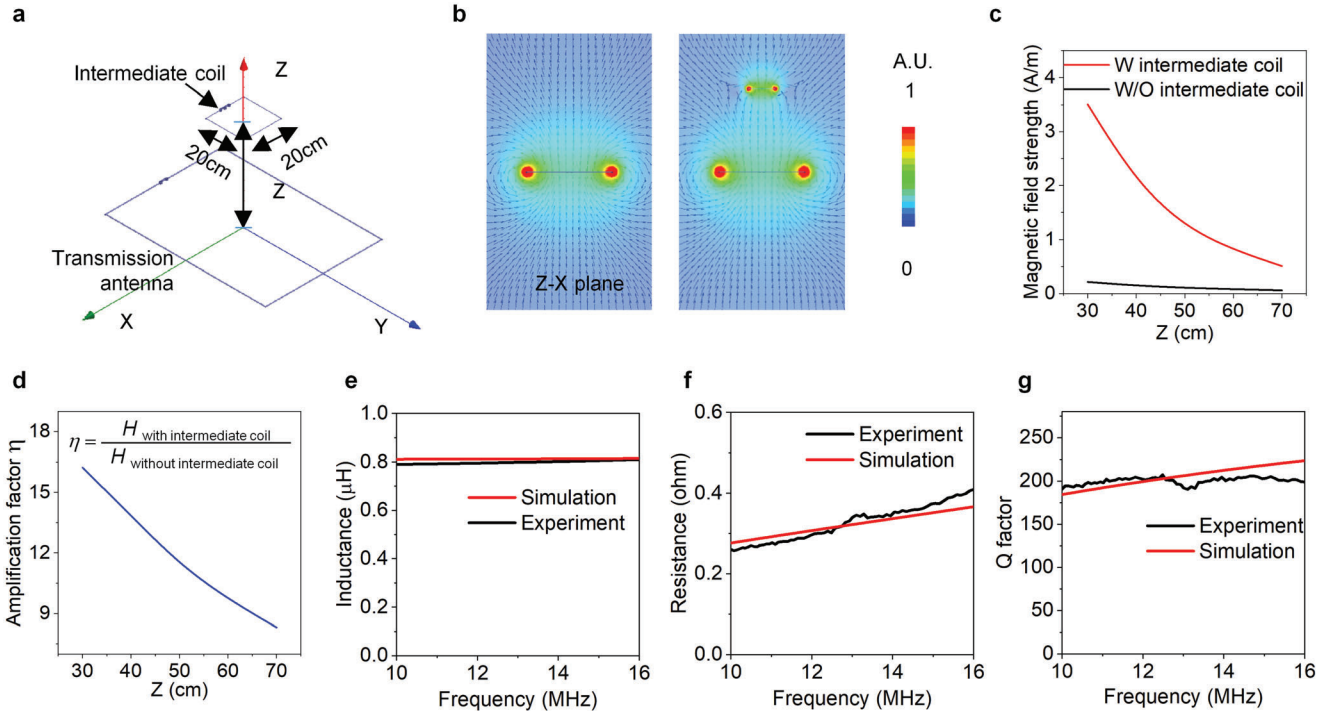

Extended Data Fig. 7 | Electrical properties of the intermediate coil. **a**, Configuration of an intermediate coil (20 cm × 20 cm, wound with Cu wire with a diameter of 0.2 mm) oriented parallel to the *X*–*Y* plane, at a distance Z from the transmission antenna. **b**, Computational results for the magnetic field distribution induced by an RF transmission antenna tuned to resonance with a receiver antenna with and without an intermediate coil. **c**, Comparison of the magnetic field strength along the *Z* direction of the transmission antenna with (W) and without (W/O) the intermediate coil. **d**, Amplification factor η along the *Z* direction of the transmission antenna with and without the intermediate coil. **e**–**g**, Simulation and experimental results for the inductance (**e**), resistance (**f**) and Q factor (**g**) as a function of frequency.

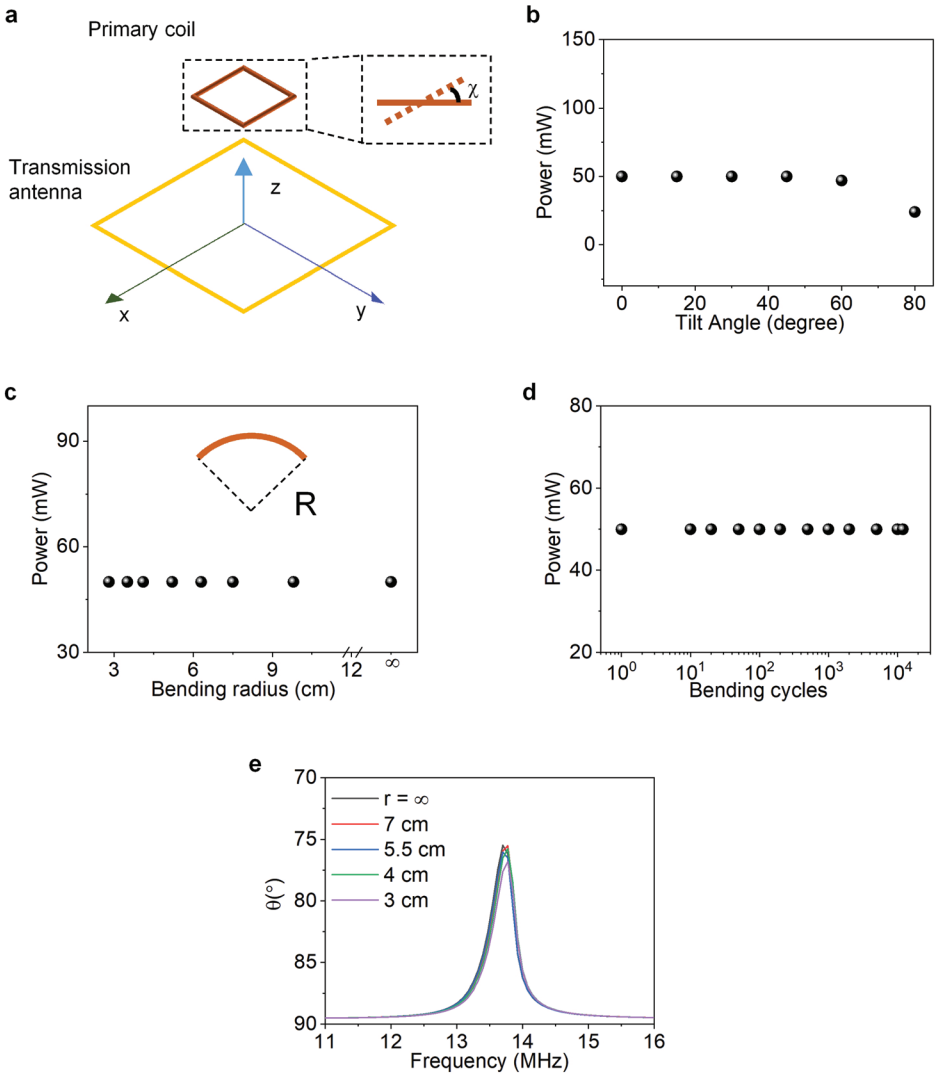

Extended Data Fig. 8 | Mechanical characterization of the epidermal VR system. a–**d**, Output power from the primary coil of an epidermal VR device as a function of tilt angle χ (**a**, geometry; **b**, data), bending radius, R (**c**) and bending cycles to an R of 2.8 cm (**d**). The distance between the device and the antenna was fixed at 20 cm for all measurements. **e**, Measured phase responses of the antennas used for wireless control over the SoCs as a function of radius of curvature. The resonance frequency is 13.56 MHz before bending. Bending induces only very slight shifts in these curves.

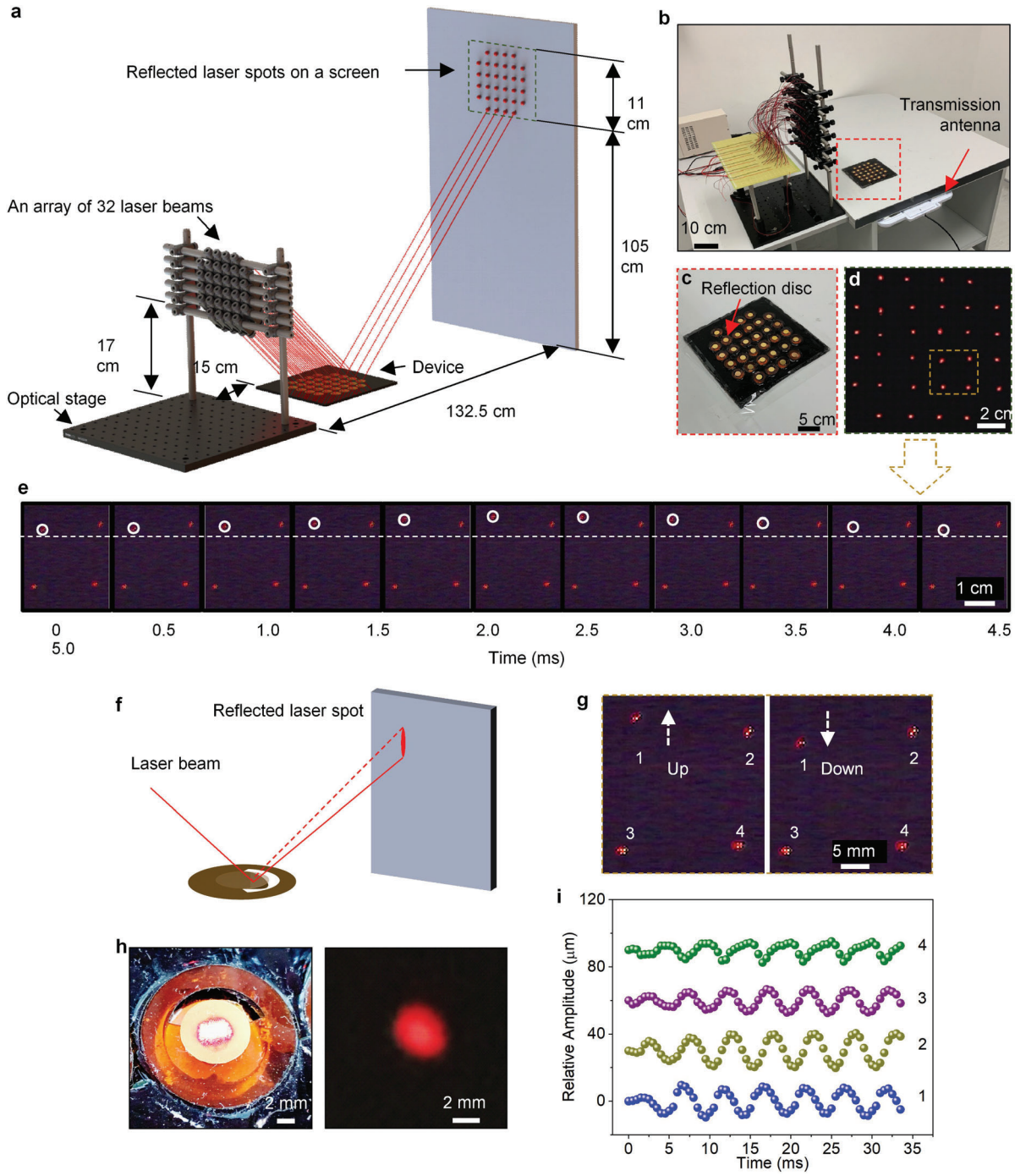

Extended Data Fig. 9 | Visualization of system level operation using an array of 32 lasers. a, Schematic illustration of a custom-built laser array system for real-time visualization of the operation of a complete epidermal VR system. **b**–**d**, The array of lasers (**b**), the corresponding array of beams reflecting from the haptic actuators, each mounted with a reflective disk (diameter of 8 mm), across an entire system (**c**), and their arrival at a monitoring screen (**d**). **e**, Representative frames extracted from video recorded using a high-speed camera to capture oscillatory motions of each of the laser spots. These motions directly determine the motions of the cantilever-based actuators. **f**, Schematic illustration of a laser spot produced by projection of a reflected beam onto a screen during the operation of the actuator. **g**, Representative frames extracted from video recorded using a high-speed camera showing the oscillatory motion of laser spot 1. **h**, Pictures of a laser spot on a reflector that mounts on a haptic actuator (left) and on the monitoring screen (right). The diameter of the laser spot is ~3 mm. **i**, Calculated displacements of four actuators determined from the measurement setup geometry and the amplitude of motion of the laser spots in **g**, **e** and Supplementary Video 4. The traces are offset in the *y* direction to facilitate visual inspection. The calculated displacements are somewhat smaller than those measured directly from individual actuators using high-speed cameras owing to slight misalignments of the lasers and to shifts in the resonance frequencies due to absence of the PDMS encapsulation layer for the devices measured using the laser technique. The results allow direct visualization and measurement of the vibration amplitudes, direction and frequency of the cantilever beams associated with each actuator across the full array.

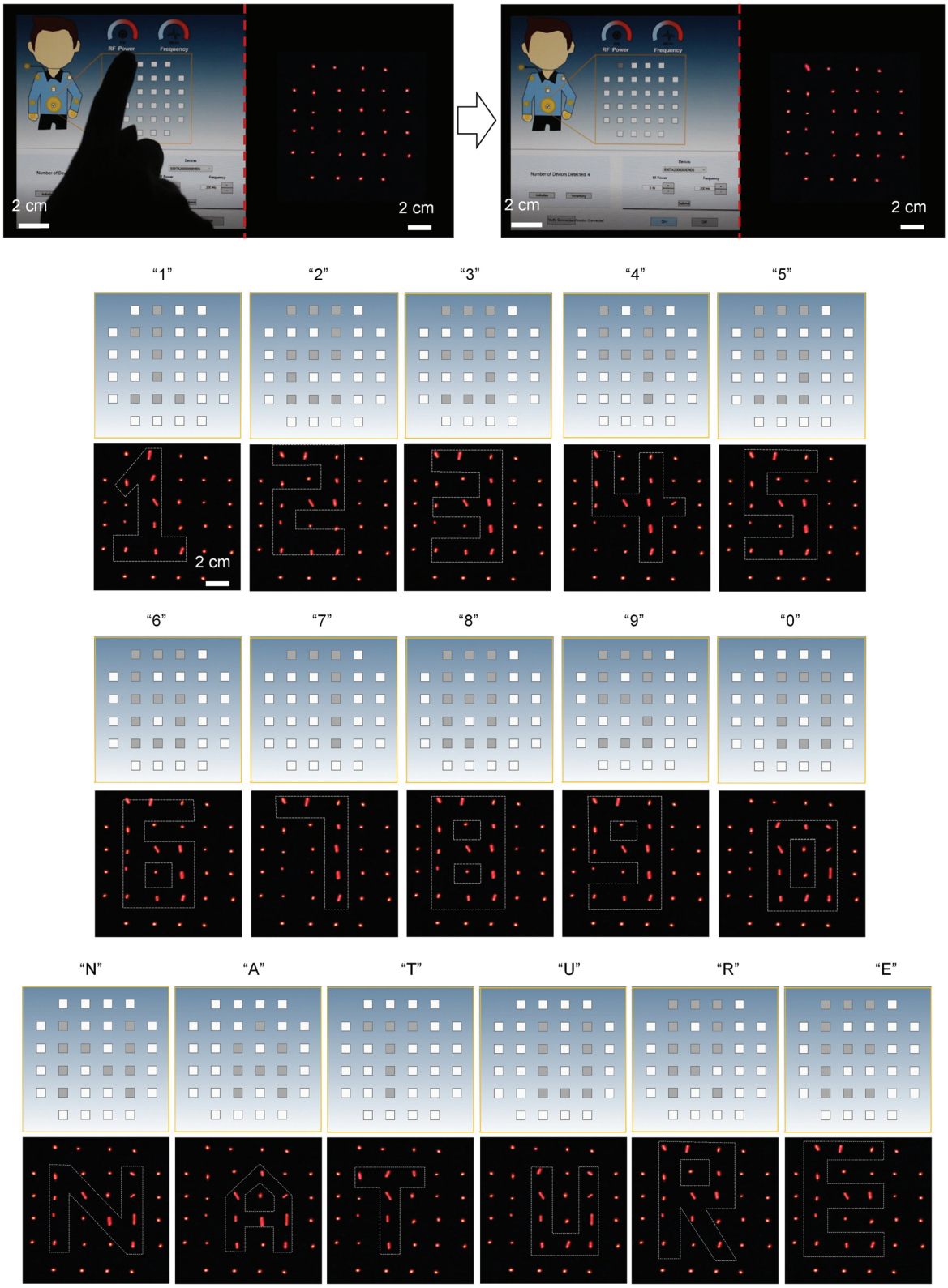

Extended Data Fig. 10 | Pictures of the operation of an epidermal VR system, visualized with a reflected array of 32 laser beams. Activation of a given haptic actuator causes the corresponding reflected spot to transform from a circular to an elliptical shape, owing to the vibratory motions (top row). The results in the lower three rows show representative spatial patterns of actuation, including numbers 0 to 9 and letters 'N', 'A', 'T', 'U', 'R' and 'E'. We note that the detailed shapes of the laser spots on the screen depend critically on the positioning of each of the beams across the corresponding reflectors mounted on the cantilevered actuator structures.

nature research

Corresponding author(s): John A. Rogers

Last updated by author(s): Jun 12, 2019

Reporting Summary

Nature Research wishes to improve the reproducibility of the work that we publish. This form provides structure for consistency and transparency in reporting. For further information on Nature Research policies, see Authors & Referees and the Editorial Policy Checklist.

Statistics

For all statistical analyses, confirm that the following items are present in the figure legend, table legend, main text, or Methods section.

n/a	Confirmed	
☐	☒	The exact sample size (*n*) for each experimental group/condition, given as a discrete number and unit of measurement
☐	☒	A statement on whether measurements were taken from distinct samples or whether the same sample was measured repeatedly
☐	☒	The statistical test(s) used AND whether they are one- or two-sided *Only common tests should be described solely by name; describe more complex techniques in the Methods section.*
☒	☐	A description of all covariates tested
☐	☒	A description of any assumptions or corrections, such as tests of normality and adjustment for multiple comparisons
☒	☐	A full description of the statistical parameters including central tendency (e.g. means) or other basic estimates (e.g. regression coefficient) AND variation (e.g. standard deviation) or associated estimates of uncertainty (e.g. confidence intervals)
☒	☐	For null hypothesis testing, the test statistic (e.g. *F*, *t*, *r*) with confidence intervals, effect sizes, degrees of freedom and *P* value noted *Give P values as exact values whenever suitable.*
☒	☐	For Bayesian analysis, information on the choice of priors and Markov chain Monte Carlo settings
☒	☐	For hierarchical and complex designs, identification of the appropriate level for tests and full reporting of outcomes
☒	☐	Estimates of effect sizes (e.g. Cohen's *d*, Pearson's *r*), indicating how they were calculated

Our web collection on statistics for biologists contains articles on many of the points above.

Software and code

Policy information about availability of computer code

Data collection	Keysight E4991B Impedance Analyzer, Labview 2016, RSR MS8229 digital multimeter, Powerlab by AD instrument.
Data analysis	MATLAB R2017b, Powerlab by AD instrument, Excel 2016, Origin 2018.

For manuscripts utilizing custom algorithms or software that are central to the research but not yet described in published literature, software must be made available to editors/reviewers. We strongly encourage code deposition in a community repository (e.g. GitHub). See the Nature Research guidelines for submitting code & software for further information.

Data

Policy information about availability of data

All manuscripts must include a data availability statement. This statement should provide the following information, where applicable:

- Accession codes, unique identifiers, or web links for publicly available datasets
- A list of figures that have associated raw data
- A description of any restrictions on data availability

All data is contained within the manuscript. Reasonable requests can be made to the corresponding author for access to the raw data.

Field-specific reporting

Please select the one below that is the best fit for your research. If you are not sure, read the appropriate sections before making your selection.

☒ Life sciences ☐ Behavioural & social sciences ☐ Ecological, evolutionary & environmental sciences

For a reference copy of the document with all sections, see nature.com/documents/nr-reporting-summary-flat.pdf

Life sciences study design

All studies must disclose on these points even when the disclosure is negative.

Sample size	Sample sizes were preliminary estimated by finite element analysis using software "Abaqus", then determined by preliminary experiments.
Data exclusions	No data were excluded.
Replication	All experiments were performed for at least 5 times. All attempts at replication were successful.
Randomization	All unit devices (actuators) were fabricated and tested first to make sure they are functional. Then integration all good devices and electronic components together to fabricate the system level devices.
Blinding	All data was collected in an unbiased manner and experiments was blinded to treatment for final analysis.

Reporting for specific materials, systems and methods

We require information from authors about some types of materials, experimental systems and methods used in many studies. Here, indicate whether each material, system or method listed is relevant to your study. If you are not sure if a list item applies to your research, read the appropriate section before selecting a response.

Materials & experimental systems

n/a	Involved in the study
☒	☐ Antibodies
☒	☐ Eukaryotic cell lines
☒	☐ Palaeontology
☒	☐ Animals and other organisms
☒	☐ Human research participants
☒	☐ Clinical data

Methods

n/a	Involved in the study
☒	☐ ChIP-seq
☒	☐ Flow cytometry
☒	☐ MRI-based neuroimaging